npj | 2D materials and applications

www.nature.com/npj2dmaterials

REVIEW ARTICLE OPEN

Check for updates

Mixed-dimensional nanocomposites based on 2D materials for hydrogen storage and CO_2 capture

Yong-Ju Park[1], Hongju Lee[1], Hye Leen Choi[1], Ma Charlene Tapia[1], Chong Yang Chuah[2,3]✉ and Tae-Hyun Bae[1]✉

Porous materials possessing high surface areas are of paramount importance in gas separation and storage, as they can potentially adsorb a large amount of gas per unit of mass or volume. Pore structure and functionality are also important factors affecting adsorbate–absorbent interactions. Hence, efforts have been devoted to developing adsorbents with large accessible surface areas and tunable functionalities to realize improvements in gas adsorption capacity. However, the gas adsorption and storage capacities of porous materials composed of a single type of building unit are often limited. To this end, mixed-dimensional hybrid materials have been developed, as they can contain more gas storage sites within their structures than simple porous materials. In this review, we discuss (1) the methods that have been used to assemble various dimensional building blocks into a range of mixed-dimensional (zero-dimensional–two-dimensional, one-dimensional–two-dimensional, and three-dimensional–two-dimensional) hybrid materials exhibiting synergistic adsorption effects, and (2) these materials' hydrogen and carbon dioxide adsorption properties and how they are correlated with their accessible surface areas. We conclude by outlining the challenges remaining to be surmounted to realize practical applications of mixed-dimensional hybrid materials and by providing future perspectives.

npj 2D Materials and Applications (2023)7:61 ; https://doi.org/10.1038/s41699-023-00425-w

INTRODUCTION

Solid adsorbents based on porous materials exhibit advantages in gas adsorption, storage, and separation processes[1,2]. The application of porous materials in carbon dioxide (CO_2) capture and hydrogen (H_2) storage is of particular interest due to the growing need for controlling greenhouse gas emissions and developing green energy. CO_2 capture can potentially be achieved via several unit operations, such as amine scrubbing, cryogenic distillation, and liquefaction[3–9]. However, these unit operations can incur a large energy penalty. Specifically, an amine-scrubbing process employs a 30–40 wt% aqueous solution of an amine, which is corrosive and has a higher heat capacity than a solid adsorbent, resulting in a large energy penalty for regeneration at an elevated temperature[3,10]. In addition, cryogenic distillation and liquefaction typically involve a phase change from gas to liquid, which requires a larger energy input than adsorptive gas separation[11]. H_2 storage is typically achieved via (1) physical storage (i.e., storage of H_2 at high pressure and/or low temperatures in designated storage vessels) or (2) material-based storage (i.e., storage as chemical hydrides and/or in porous adsorbents). In physical storage, very high-pressure compression (700–800 bar) is required to secure a high storage density, which causes several problems related to safety and cost. In comparison, storage under cryogenic conditions can achieve a high volumetric capacity at a lower cost ($12 kWh^{-1} vs. $16–19 kWh^{-1} for the compressed gas)[12]. However, there is a large energy penalty for cooling. Hence, material-based storage, which involves the capture of H_2 through physisorption (via weak van der Waals forces) or hydride formation, has been proposed as an economic alternative to physical storage.

Many types of adsorbents have been investigated for gas adsorption and storage, such as zeolites[13], metal–organic frameworks (MOFs)[3], porous organic polymers[14], mesoporous silica[15], and activated carbon[16,17], and they can be developed in various configurations (i.e., three-dimensional (3D), two-dimensional (2D), one-dimensional (1D), or zero-dimensional (0D) configurations). Each of these materials exhibits effective gas storage and separation performances upon tuning their physicochemical properties, which include but are not limited to accessible surface area and inherent porosity, thermal and mechanical stability, adsorbent–adsorbate binding energy, and density. For instance, porous materials such as zeolites and MOFs can effectively adsorb CO_2 if these materials' available binding sites are tuned via variation of silicon/aluminum (Si/Al) ratios and the generation of coordinatively unsaturated open-metal sites, respectively[3,4]. Furthermore, post-synthetic grafting of amines onto porous materials is effective for enhancing these materials' CO_2 adsorption capacities, particularly at low partial pressures[18,19].

However, adsorbents composed of only one type of porous material often have limited capacities for gas adsorption and storage. This is particularly evidenced by porous materials that lack strong, specific adsorptive forces and thus cannot effectively retain small molecules[20–22]. On the other hand, despite 2D materials (e.g., graphene-family materials) having great potential for gas adsorption and storage due to their attractive properties, such as large surface areas (~2600 $m^2 g^{-1}$) and good mechanical strengths, they inevitably exhibit sheet stacking, which leads to a decrease in their surface areas (~30 $m^2 g^{-1}$)[23–25]. Hence, several approaches, such as the synthesis of reduced graphene oxide (rGO), which is achieved through thermal treatment at various temperatures (200–800 °C))[26,27] as well as mesoporous graphene oxide (MEGO), which is developed through GO acidification, lyophilization, and annealing[28] is adopted, with the aim of increased porosities and adsorption capacities than graphene.

[1]Department of Chemical and Biomolecular Engineering, Korea Advanced Institute of Science and Technology, Daejeon 34141, Republic of Korea. [2]Department of Chemical Engineering, Universiti Teknologi PETRONAS, Bandar Seri Iskandar 32610 Perak, Malaysia. [3]CO2 Research Centre (CO2RES), Institute of Contaminant Management, Universiti Teknologi PETRONAS, Bandar Seri Iskandar 32610 Perak, Malaysia. ✉email: chongyang.chuah@utp.edu.my; thbae@kaist.ac.kr

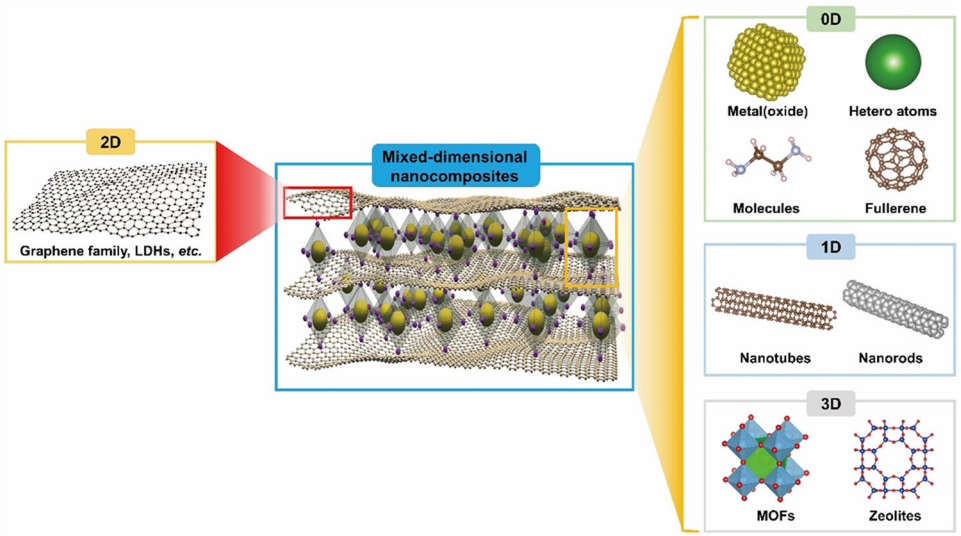

Fig. 1 Schematic of mixed-dimensional nanocomposites based on 2D materials. Mixed-dimensional nanocomposites formed from a combination of 2D and other-dimensional materials (0D, 1D, and 3D) for applications in hydrogen storage and CO_2 capture.

Nevertheless, there remains an opportunity to further enhance the gas storage and separation performance of 2D materials through the synthesis of mixed-dimensional nanocomposites[29].

To this end, efforts to improve their overall adsorptive behavior have been focused on synthesizing hybrid nanocomposite structures from two (or more) different types of adsorbents. It is expected that compared with single-material adsorbents, such hybrid nanocomposites will have (1) additional gas storage sites and thus increased gas adsorption capacities due to their syntheses involving minimal aggregation of porous adsorbents; and (2) enhanced physical and/or chemical properties, due to synergistic interactions between their two different kinds of adsorbents[20,30,31]. An attractive aspect of creating mixed-dimensional nanocomposites is the inherent ease of the process. Unlike the complex endeavor of crafting entirely novel materials, which requires significant exertion, increasing gas adsorption capacity can be achieved through the simple combination of two established materials. Furthermore, this approach opens the door to a wide range of possibilities, allowing for the exploration of various viable combinations.

Hence, in this review, we examine the applications of mixed-dimensional hybrid materials in H_2 storage and CO_2 capture processes by (1) surveying the preparation of mixed-dimensional nanocomposites to provide key insights; (2) evaluating the performance of mixed-dimensional nanocomposites in H_2 storage and CO_2 adsorption applications; and (3) examining future prospects of mixed-dimensional nanocomposites in gas separation processes. Mixed-dimensional nanocomposites, which are developed based on the combination of 0D, 1D, and 2D, are illustrated based on the following description. 0D nanomaterials are defined as those without repeated porous structures, such as elemental dopants, metals, metal oxides, fullerenes, organic molecules, and atomic clusters. In contrast, 1D nanomaterials are classified as those with one dimension that is much longer than their other two dimensions, such as nanotubes, nanorods, and nanofibers. On the other hand, 2D nanomaterials are those with sheet-like structures with traverse dimensions greater than 100 nm and thicknesses less than 5 nm, such as nanosheets and graphene. Last but not least, 3D materials have long-range-ordered porous structures (i.e., MOFs, zeolites, and element-doped MOFs) (Fig. 1).

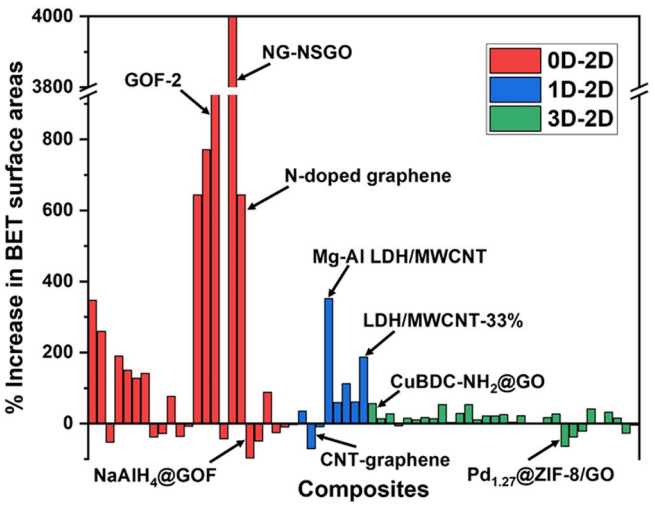

Fig. 2 Increase in BET surface area of mixed-dimensional nanocomposites. Effect of combining various mixed-dimensional materials (0D–2D, 1D–2D, and 3D–2D) on the BET surface areas of the resulting nanocomposites. The properties of several well-known adsorbents are labeled as references. The percentage increases in BET surface area are summarized in Supplementary Table 1.

RATIONALE AND PREPARATION OF MIXED-DIMENSIONAL NANOCOMPOSITES

Mixed-dimensional nanocomposites have been synthesized from their respective precursors through the manipulation of various parameters. These nanocomposites primarily comprise physical mixtures of multiple components, although chemical interactions often occur when molecules or metals are integrated into 2D materials possessing chemical functional groups. Prior to delving into the specifics of individual case studies, it is crucial to grasp the underlying rationale behind the development of such mixed-dimensional nanocomposites for their applications in gas adsorption and storage. As demonstrated in Supplementary Table 1 and Fig. 2, in general, mixed-dimensional nanocomposites possess a larger accessible area than their single-dimensional counterparts, as typically calculated by the Brunauer–Emmett–Teller (BET) method. Based on our review of the literature, ~61% of all

reported mixed-dimensional nanocomposites have demonstrated substantially greater BET surface areas than their single-dimensional counterparts. Thus, it appears that increasing the BET surface areas of mixed-dimensional nanocomposites is a prerequisite for improving their overall gas adsorption and storage capacities. Nevertheless, it should be noted that such a property may not be directly correlated to the usable capacity (also known as working capacity) in practical applications that involve repetitive adsorption/desorption cycling[32,33]. This discrepancy is potentially attributed to the existence of residual gas within the porous adsorbent that cannot be recovered during the desorption process. However, the BET surface area remains a significant physical parameter for screening porous materials intended for use in gas adsorption and storage applications.

Considering the aforementioned observations, it becomes pertinent to speculate on the potential reasons underlying the achievement of this enhanced BET surface area with the mixed-dimensional nanocomposite. This situation is notably conspicuous in MOF-based composites, as exemplified in Supplementary Table 1. In a study conducted by Liu et al.[30], the authors compared the measured composite micropore volume to the hypothetical micropore volume to investigate the porosity behavior in composite materials (specifically, HKUST-1/GO). The hypothetical micropore volume, denoted as v_n, was projected by factoring in the micropore volumes of GO and HKUST-1 (v_{GO} and $v_{HKUST-1}$), as well as the fraction of each component (X_{GO} and $X_{HKUST-1}$) within the composites (Eq. 1). The investigation revealed that the measured micropore volume of the HKUST-1/GO composites, particularly at the optimal GO content (3 wt% and 9 wt%), surpasses the values anticipated from Eq. 1. It has been postulated that the inclusion of GO has impeded the aggregation of HKUST-1 crystallites, thereby fostering improved dispersion and an amplified accessible surface area. This phenomenon has been observed in numerous other studies, as documented in Supplementary Table 1.

$$v_n = v_{GO} \times X_{GO} + v_{HKUST-1} \times X_{HKUST-1} \quad (1)$$

However, it is imperative to note that the types of materials, composition, and synthesis methods must be meticulously optimized. This is essential since the overall structure of the composites can undergo substantial distortion, resulting in a significant reduction in surface area. For instance, an excessive quantity of GO can impede the growth of specific MOFs, consequently yielding poor crystallinity of the MOF material. Hence, in the subsequent section, a general summary of the process used to fabricate several mixed-dimensional nanocomposites is elaborated.

Preparation of 0D–2D composites

A deposition method is typically used to prepare 0D–2D composites, whereby the outer surface of 2D materials is decorated with judiciously selected functionalities (e.g., metals) to promote gas adsorption[34]. In a typical procedure, two stocks—a solution of metal ions and a solution (suspension) of a 2D material—are prepared and then mixed. Sonication of this mixture is then performed to achieve a uniform dispersion of metal ions, followed by a reduction reaction under pressurized conditions. The successful formation of 0D–2D composites can be verified using X-ray diffraction (XRD) analysis. For instance, Zhou et al.[34] prepared nickel (Ni)/graphene composites via a multiplex reduction reaction of a nickel(II) hydroxide/graphene precursor ($Ni(OH)_2$/graphene). The conversion of $Ni(OH)_2$ to Ni in the graphene matrix was confirmed by the disappearance of $Ni(OH)_2$ peaks in the XRD pattern of the Ni/graphene nanocomposite, as shown in Fig. 3a.

Alternatively, material doping can be employed for the construction of 0D–2D mixed-dimensional nanocomposites, with a commonly adopted doping approach being electroless deposition. This involves an autocatalytic chemical reduction in which metal ions are deposited onto a surface without the application of electrical energy. This approach is effective for creating a uniform coating, even on a non-conductive surface. For example, Huang et al.[35] electroless deposited platinum (Pt) or palladium (Pd) particles onto the surface of graphene oxide (GO) via the reduction of Pt^{5+} and Pd^{2+} to metallic Pt and Pd, respectively. As indicated in Fig. 3b, the successful fabrication of Pt-doped graphene was clearly confirmed by the XRD pattern. However, the characteristic peak for Pd-doped graphene was not observed, which may have been due to the smaller particle size of Pd (<5 nm) and lower Pd content (~2.2 wt%) compared with those for Pt-doped graphene.

Preparation of 1D–2D composites

1D–2D composite materials are generally synthesized through the physical blending of pre-existing constituents. Therefore, the synthesis procedure is relatively straightforward: combining two components within a solution mixture, followed by fabrication or casting, and subsequent solvent removal. Ensuring a uniform dispersion is pivotal, often achieved through sonication. Solvent removal can be accomplished via evaporation or filtration, particularly when the composite is formed on a porous membrane substrate. Aboutalebi et al.[36] synthesized a 1D–2D nanocomposite comprising a combination of GO and multi-walled carbon nanotubes (MWCNTs) via mixing. They found that the addition of MWCNTs into a GO suspension could promote the reduction of GO due to the presence of residual oxidative debris on the surface of MWCNTs[37,38]. The reduction of GO was confirmed by a decrease in the proportion of epoxy/hydroxyl groups compared with the proportions of carboxylate and carbonyl groups, based on X-ray photoelectron spectroscopy (XPS) analyses of GO and GO/MWCNTs (Fig. 3c, d). Alternatively, 1D–2D nanocomposites can be formed through an exfoliation–self-assembly approach. Wang et al.[39] employed this approach by mixing suspensions of a layered double hydroxide (LDH) and oxidized carbon nanotubes (OCNTs). The resulting mixture underwent self-assembly as the LDH was positively charged, and the OCNTs were negatively charged. This approach has been adopted in many other studies using a variety of 1D and 2D materials[40,41].

Another approach used to form 1D–2D nanocomposites is co-precipitation, which employs precursors that are soluble in an original solution but insoluble in the mixture where the nanocomposites are formed. Wang et al.[39] co-precipitated an LDH and OCNTs to make 1D–2D composites by adding LDH precursors into a highly dispersed solution of OCNTs. Compared with exfoliation/self-assembly, co-precipitation is better, as it results in nanocomposites with greater dispersion of LDH molecules. This is attributed to the presence of negatively charged OCNTs that limit the growth of LDHs[39,42].

Preparation of 3D–2D composites

The synthesis of 3D–2D nanocomposites is typically conducted via an in situ growth (co-precipitation) method, as elucidated in Section 2.2[43]. The process is summarized in Fig. 3e and involves (a) preparation of a homogeneous solution containing precursors of the 3D adsorbents, (b) incorporation of a 2D material into the homogenous precursor solution, and (c) synthesis of 3D adsorbents in the presence of the 2D material[43,44]. Compared with mixing two building blocks that have been made separately, this method affords a more uniform growth of 3D adsorbent on 2D sheets, leading to a greater increase in accessible surface area in the resulting mixed-dimensional nanocomposite. For instance, Li et al.[43] formed a 2D–3D nanocomposite through the growth of Ni-MOF-74 (NiDOBDC) nanocrystals with a uniform particle size on GO sheets. The latter facilitated the growth of NiDOBDC

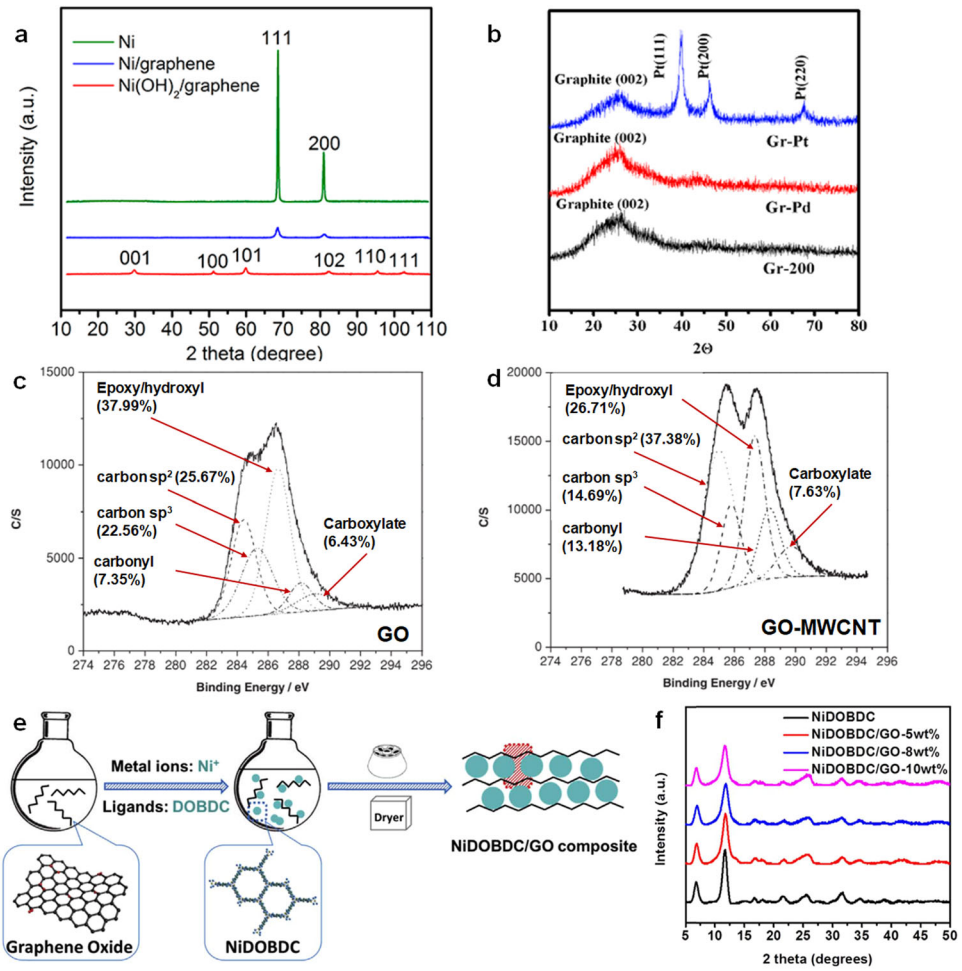

Fig. 3 Preparation of mixed-dimensional nanocomposites. a Comparison of XRD patterns of metallic Ni, $Ni(OH)_2$/graphene, and Ni/graphene. This scanning is carried out at room temperature using a diffractometer equipped with Cu Kα radiation ($\lambda = 0.154$ nm). **a** is reprinted with permission from ref. [34], Copyright 2016 American Chemical Society. **b** XRD patterns of metal–graphene composites (Gr–Pt, Gr–Pd) and graphene (Gr-200). The scanning is conducted at ambient temperature. **b** is reprinted with permission from ref. [35], Copyright 2011 Elsevier. **c**, **d** XPS spectra of GO and GO-MWCNT in the carbon region. The deconvolution of C1s spectra was carried out using software that utilizes a Gaussian–Lorentzian peak fitting method, following background correction. **c**, **d** are reprinted with permission from ref. [36], Copyright 2012 Wiley-VCH Verlag GmbH & Co. **e** Reaction scheme for the synthesis of NiDOBDC/GO composites via in-situ growth process. This is accomplished by heating at 100 °C for 2 h, employing N,N′-dimethylformamide as the organic solvent. **f** XRD patterns of NiDOBDC/GO composites. This scanning is carried out at room temperature using a diffractometer equipped with Cu Kα radiation ($\lambda = 0.154$ nm). **e**, **f** are reprinted with permission from ref. [43], Copyright 2018 Elsevier.

nanocrystals, leading to the creation of 3D nanoarchitectures that retained the porous nature of NiDOBDC. As shown in Fig. 3f, the crystal structure of the MOF remained intact within the NiDOBDC/GO composites. Moreover, the aggregation of NiDOBDC nanocrystals was inhibited, which enhanced the overall gas storage capacity of the 2D–3D nanocomposite.

VARIOUS MIXED-DIMENSIONAL NANOCOMPOSITES FOR H_2 STORAGE AND CO_2 CAPTURE

The applicability of mixed-dimensional nanocomposites to gas adsorption has been extensively investigated by various researchers. One of the noteworthy advantages observed in adsorption, when compared to other conventional approaches such as cryogenic distillation and amine scrubbing, is its utilization of a relatively lower energy penalty. Cryogenic distillation, in particular, demands intricate equipment design to ensure the attainment of requisite operating conditions (high pressure and low temperature) for achieving elevated CO_2 and H_2 purity levels. On the other hand, amine scrubbing, reliant on chemical adsorption via amines, is often plagued by a range of limitations. These include the unwelcome issue of vessel corrosion and the substantial energy requirement for regeneration. Additionally, the significant presence of water within the solution contributes substantially to the energy costs due to water's high heat capacity. For a more comprehensive understanding, readers can turn to the thorough comparison of each unit operation conducted by Chuah et al.[2,4]. Thus, this section gives an overview of the performance of mixed-dimensional nanocomposites in H_2 and CO_2 adsorption processes. Detailed performance data can be found in Supplementary Table 2.

0D–2D composites

Typically, 0D materials are incorporated into 2D materials to increase the binding energy (i.e., isosteric heat of adsorption ($-Q_{st}$)) of the target gas and control the interlayer spacing of the 2D sheets. The 0D materials that have been widely investigated are heteroatoms, such as nitrogen (N) and boron (B); transition metals; metal oxides; and noble metals[45]. The H_2 storage and CO_2

capacity of such 0D–2D composites are discussed in the following sections.

H_2 adsorption and storage. The synthesis of 0D–2D composites possessing high H_2 storage capacities can be achieved by effectively controlling the surface areas and energies of interaction between 0D and 2D materials. For example, Kumar et al.[46] applied microwave irradiation to form nanoholes (~10 nm) in the basal plane of graphene and thus obtained nanoporous graphene sheets, which they treated with Pd nanoparticles to afford Pd-embedded 3D nanoporous graphene (3D Pd-E-PG) (Fig. 4a). Compared with pristine GO, the BET surface area and H_2 storage capacity of 3D Pd-E-PG at 77 K and 70 bar were increased by 77% and 260%, respectively (Fig. 4b). Such enhanced H_2 adsorption was attributable to a spillover mechanism (i.e., the dissociation of H_2) that is commonly observed in heterogeneous catalysis[47,48]. Similarly, Huang et al.[35] observed a spillover mechanism-induced increase in H_2 adsorption when Pd or Pt nanoparticles were incorporated into GO layers to generate Pt/GO and Pd/GO nanocomposites, respectively. In contrast to pristine GO, which showed an H_2 adsorption of 0.076 wt% at 303 K and 57 bar, their Pt/GO and Pd/GO nanocomposites exhibited far higher H_2 adsorption values of 0.15 wt% and 0.156 wt%, respectively, under the same conditions. Kostoglou et al. used plasma-induced exfoliation to form nanoporous few-layer graphene (FLG), which they then decorated with Pt nanoparticles and subsequently reduced via a thermal process[49]. The resulting Pt/FLG nanocomposite exhibited a higher H_2 adsorption capacity (0.131 wt%) than that of pristine FLG (0.084 wt%) at 298 K and 20 bar (Fig. 4c).

Other metals, such as Ni and iron (Fe) nanoparticles, have also been adopted to develop 0D–2D nanocomposites. Ismail et al. synthesized two different types of nanocomposites by doping Ni or Pd nanoparticles into graphene sheets[50]. The integration of these nanoparticles onto the graphene sheets has resulted in an increase in hydrogen storage capacity at low temperatures (80 K), yielding values of 2.8 wt% for Pd-RGO and 2.7 wt% for Ni–RGO nanocomposites, respectively, as compared to the capacity of 1.9 wt% exhibited by pure graphene. However, when exposed to elevated temperatures of 300 K, unlike Pd, Ni doping did not enhance the H_2 adsorption capacity (Fig. 4d). While the reason behind this phenomenon remained unclear, a hypothesis was put forth suggesting that the presence of Ni in oxide and hydroxide forms within rGO might restrict the accessibility of H_2 to the available active sites in Ni-RGO nanocomposites at higher temperatures. In another study, Ni nanoparticles and hierarchical 3D porous rGO (3DHPG-Ni) were combined to form 0D–3D nanocomposites[51]. In this case, poly(methyl methacrylate), which could be removed by a calcination process, was used as a sacrificial template to increase the BET surface area to as high as 925 $m^2 g^{-1}$. The use of 7.5 wt% Ni in the nanocomposite material enabled the maximum H_2 adsorption capacity to be realized at 5 bar and 77 K (Fig. 4e). However, further increases in the Ni nanoparticle loading resulted in a drastic decrease in H_2 adsorption capacity, which was ascribed to decreases in accessible surface area, micropore volume, and mesopore volume. Hudson et al.[52] incorporated Fe nanoclusters into graphene sheets to create Fe/GS composites, which showed a 58% higher H_2 adsorption capacity than pristine GO at 27 °C and 50 bar (Fig. 4f).

Aside from noble metals, alternative 0D materials have been combined with 2D materials to generate mixed-dimensional nanocomposites for applications in H_2 storage. For example, Wang et al.[53] employed Ni–B nanoalloys as 0D materials in combination with graphene to develop 0D–2D composites. The optimization of the Ni and B content in graphene (0.83 wt% Ni and 1.09 wt% B; GP-$Ni_{0.83}$-$B_{1.09}$) led to an H_2 storage capacity of 4.4 wt% at 1 bar and 77 K, which was approximately three times that of pristine GO under these conditions. This enhancement was attributed to an increase in the interaction between GP–$Ni_{0.83}$–$B_{1.09}$ and H_2, despite the drastic decrease in BET surface area with respect to pure GO. Ariharan et al. examined the H_2 storage potential of N-doped graphene, which they synthesized via a hydrothermal reaction and thermal annealing process[54]. N-doped graphene exhibited substantially higher accessible surface area and overall porosity than pure GO (78 $m^2 g^{-1}$ vs. 580 $m^2 g^{-1}$). Consequently, the H_2 adsorption capacity of N-doped graphene at 25 °C and 90 bar was ~1.5 wt%, significantly greater than that of GO under these conditions.

Integration of 0D materials onto 2D structures, extending beyond graphene to include transition metal oxides, has also been undertaken. However, such experimental investigations are relatively less prevalent when compared to studies involving graphene. In a study conducted by Huang et al.[55], magnesium (Mg) metal powders were subjected to ball milling with iron oxides (Fe_2O_3 and Fe_3O_4) to explore their potential enhancement in H_2 storage properties. The incorporated transition metals function as catalysts to enhance hydrogen absorption/desorption kinetics. Nevertheless, during the hydrogen storage process, both iron oxides undergo a reduction process, resulting in the formation of pure iron and consequently leading to a decline in H_2 storage capacity upon rehydrogenation. Nonetheless, further analyses of the developed adsorbents through multiple cycling processes for H_2 regeneration have unveiled a significantly more pronounced decrease in H_2 storage capacity for rehydrogenated Mg/Fe_2O_3 in comparison to Mg/Fe_3O_4. This difference is likely attributed to a comparatively higher amount of Mg within the Mg/Fe_2O_3 composite as opposed to the Mg/Fe_3O_4 composite.

Computational simulations were employed to evaluate whether 0D–2D nanocomposites can achieve an H_2 adsorption capacity of 5.5 wt% at ambient temperature[56], which is a standard set by the U.S. Department of Energy. As summarized in Supplementary Table 3, lithium (Li)-based 2D nanocomposites were found to have a high H_2 adsorption capacity. Zhang et al.[57] showed by density functional theory (DFT) calculations that decorating a graphene surface with Li atoms could increase its H_2 adsorption capacity to 6.94 wt% under ambient conditions. Similarly, Luo et al. performed a DFT analysis of the decoration of rGO with Li atoms, which revealed that Li oxide/Li hydroxide (Li_4O/Li_3OH) clusters would be formed and bound strongly on the rGO substrate, thereby leading to increases in both H_2 binding energy and H_2 adsorption capacity (~10.26 wt%) at near ambient temperature (Fig. 5a)[58]. They found that each Li atom in Li_4O/Li_3OH would adsorb at least two H_2 molecules with an adsorption energy of −0.20 eV/H_2. Hussain et al.[59] incorporated other light metals, such as sodium (Na), potassium (K), and calcium (Ca), into boron-graphdiyne (BGDY) nanosheets. The binding energy between the metal dopants and the BGDY monolayer (~−2.85 eV) was found to be higher than their corresponding cohesive energy (~−1.38 eV) (Fig. 5b). Moreover, BGDY nanosheets doped with Li, Na, K, and Ca had H_2 storage capacities of 14.29 wt%, 11.11 wt%, 9.10 wt%, and 8.99 wt%, respectively, under ambient conditions, which were higher than those of the untreated BGDY nanosheets and other commonly adopted metal-doped 2D materials[59]. This result is consistent with the minimum dopant–dopant distances of 4.45 Å, 5.16 Å, 5.20 Å, and 4.86 Å for Li, Na, K, and Ca, respectively. The shortest dopant–dopant distance was in BGDY@Li and is presumably attributable to Li having the smallest ionic radius of all of the metal dopants tested. These findings were subsequently proven by other researchers who have reported the outstanding H_2 storage performance of 2D light-metal nanocomposites[60,61].

Simulation studies were also performed on a sandwiched graphene–fullerene composite (SGFC) that had a pillared graphene structure, in which fullerene was randomly dispersed between parallel graphene layers. Compared with non-sandwich nanocomposites, SGFC had additional micropores and mesopores, which endowed it with a reasonably high surface area (up to 685 $m^2 g^{-1}$) and H_2 adsorption capacity (3.79 wt%) at 77 K and 1 bar[62]. A further enhancement in H_2 storage capacity was achieved by introducing Li

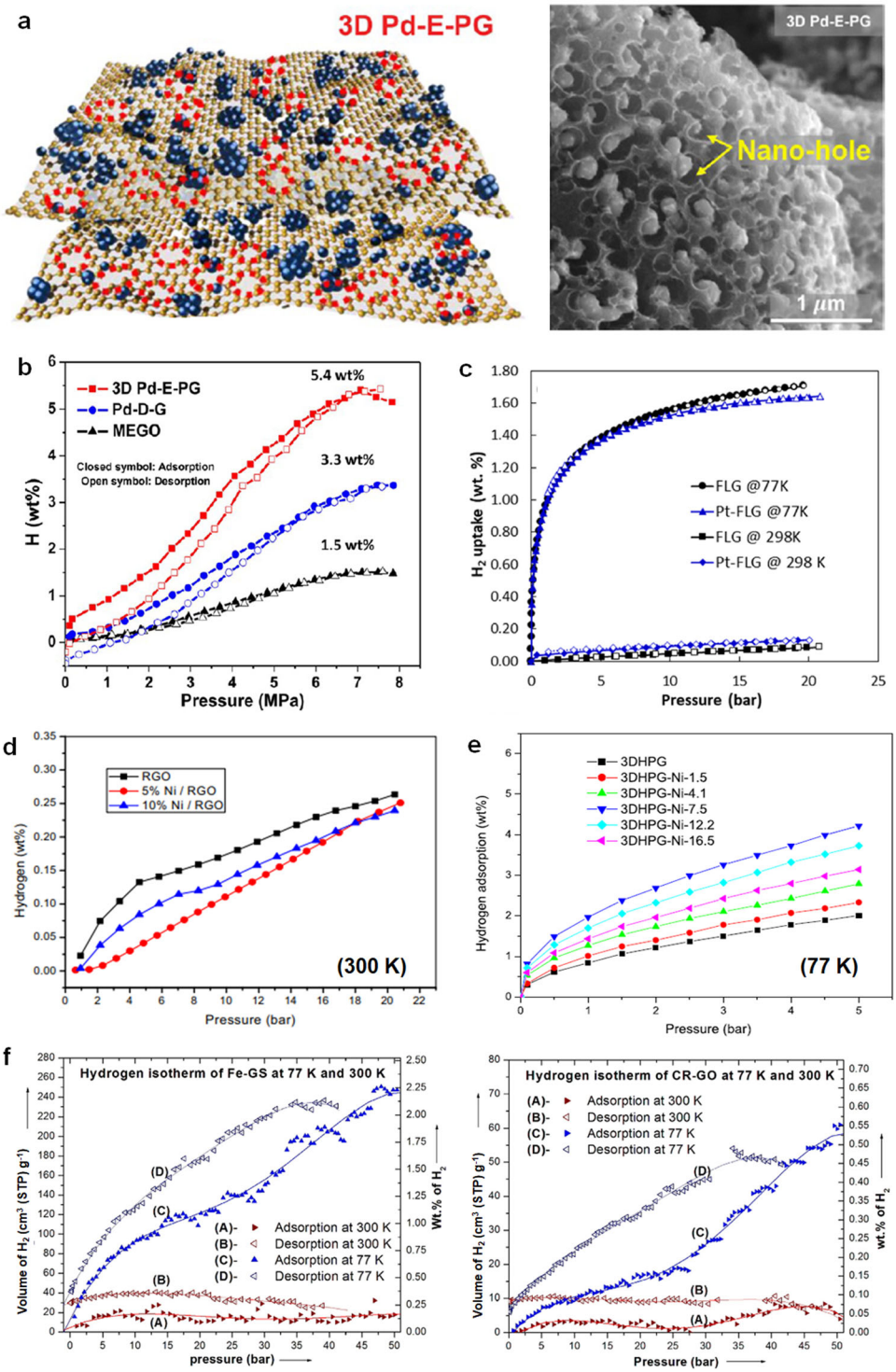

Fig. 4 Hydrogen storage in 0D-2D nanocomposites. a Schematic illustration and SEM image of 3D Pd-E-PG. This adsorbent is synthesized via microwave irradiation at 900 W for 60 s. **b** High-pressure H_2 adsorption isotherms of 3D Pd-E-PG, Pd-D-G, and MEGO at 77 K. **a**, **b** are reprinted with permission from ref. [46], Copyright 2015 American Chemical Society. **c** H_2 adsorption isotherms of FLG and Pt-decorated FLG powder at 77 K and 298 K, respectively. **c** is reprinted with permission from ref. [49], Copyright 2021 Elsevier. **d** H_2 adsorption isotherms of Ni-RGO composites at 300 K. **d** is reprinted with permission from ref. [50], Copyright 2015 Elsevier. **e** High-pressure H_2 adsorption isotherms of 3DHPG-Ni based nanocomposites at 77 K. **e** is reprinted with permission from ref. [51], Copyright 2015 Elsevier. **f** H_2 adsorption–desorption isotherms of CR-GO (chemically reduced GO) and Fe–GS (graphene sheets with Fe nanoclusters) at 77 K and 300 K, respectively. **f** is reprinted with permission from ref. [52], Copyright 2014 Elsevier.

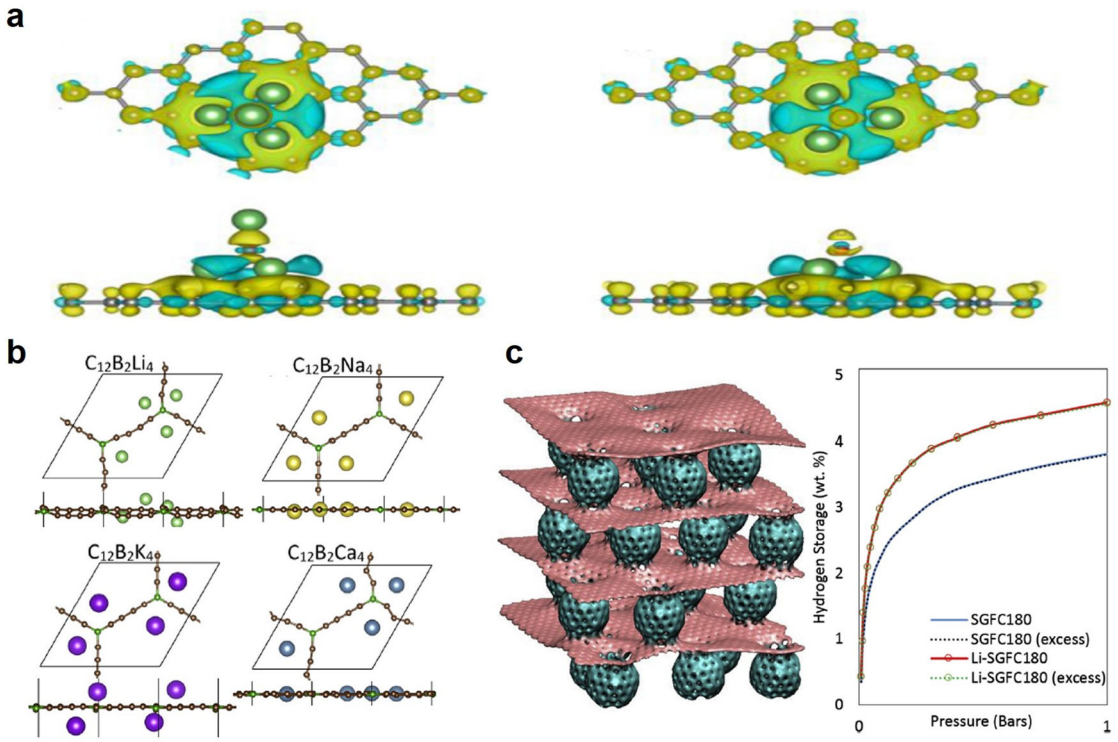

Fig. 5 Simulations on hydrogen storage in 0D–2D nanocomposites. a Charge density difference between Li_4O (left) and Li_3OH (right) clusters bound on graphene surfaces. **a** is reprinted with permission from ref. [58], Copyright 2019 Elsevier. **b** Optimized structures of BGDY@4Li, BGDY@4Na, BGDY@4 K, and BGDY@4Ca in top and side views. C, B, Li, Na, K and Ca are shown in brown, dark green, light green, yellow, purple, and blue, respectively. The calculation is performed using V **b** is reprinted with permission from ref. [59], Copyright 2019 Elsevier. The calculations are carried out utilizing the density functional theory (DFT) approach, employing the Vienna ab initio simulation package (VASP). **c** Proposed structure for SGFC and its H_2 storage performance (at 77 K) with and without Li doping. **c** is reprinted with permission from ref. [62], Copyright 2016 Elsevier.

ions; as shown in Fig. 5c, Li-doped SGFC exhibited an H_2 storage capacity as high as 5.06 wt% at 77 K and 1 bar.

CO_2 adsorption. Numerous studies have applied 0D–2D composites to capture CO_2. First, metal oxide/GO composites were investigated for potential applications in CO_2 capture, given their abundant oxygen functionalities[63,64]. For instance, Chowdhury et al.[65] employed a one-step colloidal blending method to disperse titanium oxide (TiO_2) nanoparticles in a GO solution, which afforded mesoporous (TiO_2)/GO nanocomposites. Field-emission scanning electron microscopy of these nanocomposites showed that the TiO_2 nanoparticles were uniformly distributed in GO laminates at a relatively low loading of TiO_2, i.e., 10 wt% TiO_2, and thus this nanocomposite was denoted TiO_2/GO-0.10. (Fig. 6a) The CO_2 adsorption capacity of TiO_2/GO-0.10 was 2.25 mmol g^{-1} at 1 bar and 0 °C, and its zero-coverage heat of adsorption ($-Q_{st}$) was relatively low (19.6 kJ mol^{-1}) compared with those of other well-studied adsorbents, such as zeolites and MOFs (20–50 kJ mol^{-1}). (Fig. 6b)

Amine-crosslinked graphene adsorbents, which we consider to be 0D–2D materials, have also been investigated for applications in CO_2 capture[66]. The adjustment of the interlayer spacing of GO by the addition of various amines as crosslinkers (e.g., ethylenediamine (EDA), 1,4-butanediamine, and 1,6-hexanediamine) led to enhancements in CO_2 adsorption capacity (Fig. 6c, d). In addition, there was a positive correlation between the length of the crosslinker and the interlayer distance in the resulting nanocomposites. An increase in the loading of the amine linker could also increase the interplanar distance; for example, as the EDA loading in GO-EDA increased from 0 to 0.5 mL, the interlayer spacing increased from 0.762 to 0.917 nm. A change in the interlayer spacing also affected the CO_2 adsorption capacities of the nanocomposites, with the highest CO_2 adsorption achieved at an intermediate interlayer spacing (0.86–0.88 nm). This was attributed to the presence of the strongest GO–CO_2 interaction at this optimal spacing (interaction energy = ~45 kJ mol^{-1}); in comparison, other nanocomposites were reported to exhibit weaker GO–CO_2 interactions (20 kJ mol^{-1})[67]. Similarly, Chen et al.[68] developed benzylamine-crosslinked GO (GOF-1) and *p*-xylylenediamine-crosslinked GO (GOF-2), as shown in Fig. 6e, f. The interlayer spacings of GOF-1 (0.90 nm) and GOF-2 (1.02 nm) were larger than those of GO-EDA mentioned above. In addition, a high amine concentration in GO allowed the resulting composite to have a CO_2 adsorption capacity and CO_2/N_2 selectivity of 1.52 mmol g^{-1} and 19.2, respectively, at 1 atm and 0 °C, which are higher than those of pure GO (1.10 mmol g^{-1} and 32.3). Rodríguez-Gracía et al.[69] fabricated a GO/polyaniline nanocomposite, which had a higher recyclability and CO_2 adsorption capacity at high pressures than pristine GO.

1D–2D nanocomposites

Similar to 0D nanomaterials, 1D nanomaterials, including but not limited to nanotubes, nanorods, and nanofibers, act as "spacers" in 2D materials, that is, 1D nanomaterials intercalate with 2D nanomaterials and thereby modify the interlayer spacing of nanosheets. This can create additional spacing between nanosheets, meaning that a combination of 1D and 2D nanomaterials synergistically interacts to enhance the transport of gas molecules. Therefore, compared with the active sites in 2D nanomaterials, the active sites in 1D–2D nanocomposites are more accessible, which improves the adsorption of gas molecules into 1D–2D composites[70]. Hence, it is expected that changes in the weight percentages of the 1D spacer and 2D nanomaterial in a

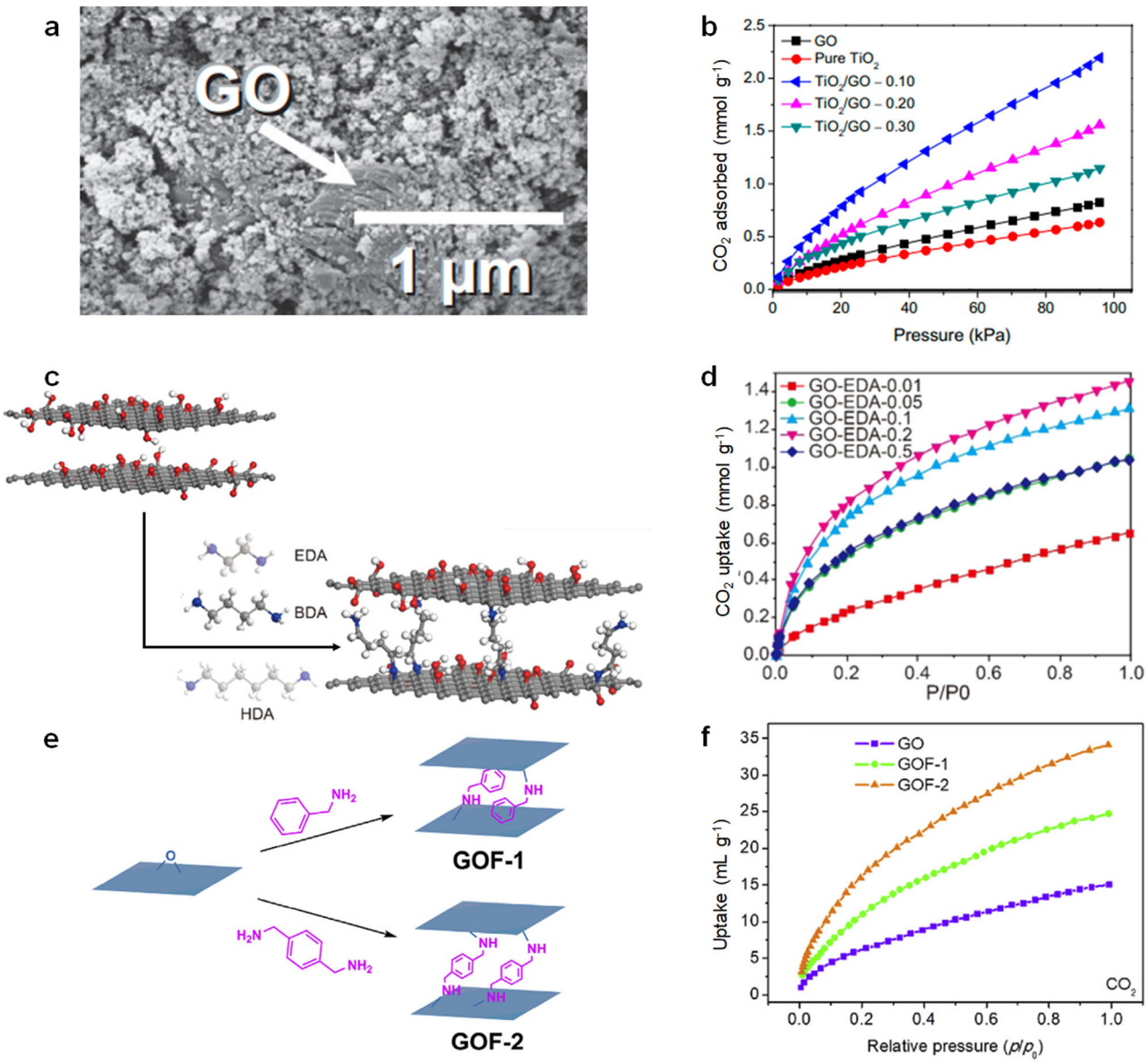

Fig. 6 CO_2 capture in 0D-2D nanocomposites. a SEM images of GO TiO_2/GO-0.10. **b** CO_2 adsorption isotherms of GO, TiO_2, TiO_2/GO-0.10, TiO_2/GO-0.20, and TiO_2/GO-0.30 at 0 °C. **a**, **b** are reprinted with permission from ref. [65], Copyright 2015 Elsevier. **c** Intercalation of various amines (EDA, BDA, and HDA) into GO layers conducted at 70 °C for 6 h, and **d** the CO_2 adsorption isotherms of EDA-GO composites at 25 °C. **c, d** are reprinted with permission from ref. [66], Copyright 2019 Elsevier. **e** Intercalation of benzylamine (GOF-1) or *p*-xylylenediamine (GOF-2) into GO, conducted by solvothermal treatment of GO at 80 °C for 4 h with benzylamine, and **f** CO_2 adsorption isotherms at 0 °C. **e**, **f** are reprinted with permission from ref. [68], Copyright 2019 Elsevier.

1D–2D nanocomposite can affect its gas adsorption capacity and long-term stability[42,71].

Among the most representative examples of 1D structures that have been applied in 1D–2D composites are CNTs. CNTs possess good mechanical properties and electrical and thermal conductivities, all of which can be tuned with appropriate changes in CNT diameter, CNT length, and the number of CNT walls. CNTs are utilized in various fields, such as in gas storage/adsorption, energy conversion and storage devices, and in chemical sensors[72–75]. CNTs also minimize restacking of individual 2D GO sheets, which suggests that they could be used to obtain materials with enhanced gas adsorption performance.

H_2 adsorption and storage. Aboutalebi et al.[36] found that the intercalation of MWCNTs into GO resulted in a material with a higher H_2 adsorption capacity (2.6 wt%) than those of various MOFs (e.g., IRMOF-1, SNU-5, and MOF-177) and carbon-based materials (e.g., activated carbon, GO and single-walled carbon nanotubes (SWCNTs)) under comparable conditions (25 °C and 50 bar) (Fig. 7a). It was observed that the introduction of MWCNTs did not affect the ordering of GO sheets; rather, MWCNTs served as spacers between GO layers to prevent uncontrolled restacking of GO layers (Fig. 7b). In addition, GO that was synthesized via a liquid crystal method possessed a well-defined layered structure with an interlayer spacing of ~0.8 mm, which provided accessible open carbon sites on the GO surface for the accommodation and intercalation of hydrogen atoms. Furthermore, MWCNT-GO composites exhibited substantially less bundling than MWCNTs, thus ensuring uniform dispersion onto the surface of GO.

Wu et al.[76] used molecular dynamics simulations to investigate the gas adsorption performance of MWCNT-GO composites

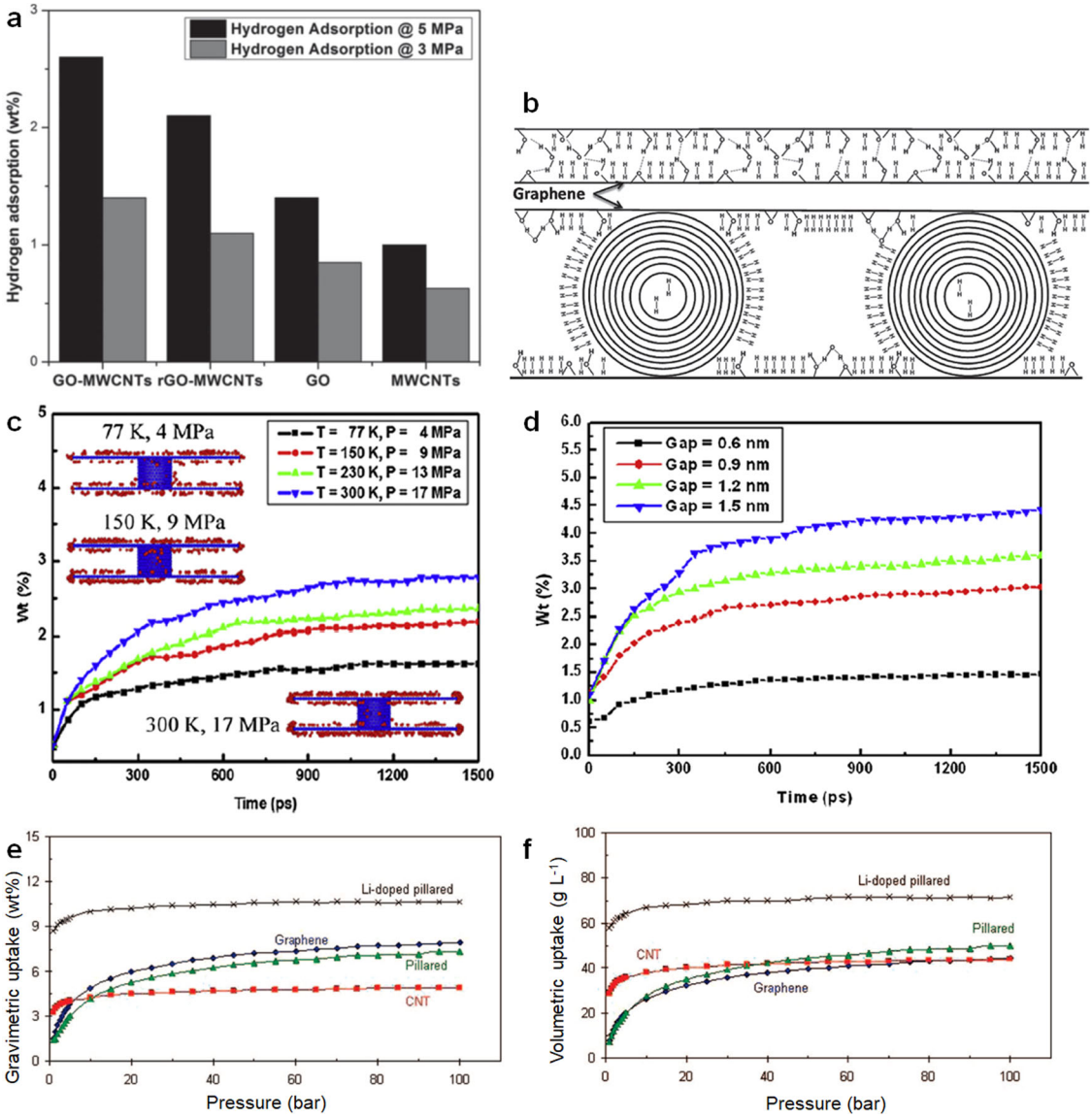

Fig. 7 Hydrogen storage in 1D-2D nanocomposites. a Comparison of H_2 adsorption by four nanocomposite frameworks (GO-MWCNT, rGO-MWCNT, GO, and MWCNT) under various pressures and room temperature. **b** Schematic comparison of H_2 adsorption of GO and GO/MWCNT nanocomposites. **a**, **b** are reprinted with permission from ref. [36], Copyright 2012 Wiley-VCH Verlag GmbH & Co. **c** Gravimetric H_2 adsorption over time at various temperatures (77 K, 150 K, 230 K, and 300 K). **d** Effect of variation in gap size (0.6–1.5 nm) on gravimetric H_2 storage. **c**, **d** are reprinted with permission from ref. [76], Copyright 2012 Elsevier. The calculations in **c**, **d** are performed using molecular dynamics simulation. **e**, **f** Comparison of gravimetric and volumetric H_2 adsorption of graphene, CNT, pillared graphene and Li-doped pillared graphene at 77 K. **e**, **f** are reprinted with permission from ref. [70], Copyright 2008 Elsevier.

having a pillared graphene form. This structure was chosen as it has a high surface area and storage capacity. The operating parameters were chosen to optimize the pressure, temperature, and geometric structures of pillared graphene. Regarding pressure and temperature, the MWCNT-GO composites' H_2 storage performance was found to be consistent with their thermodynamic behavior due to the exothermic nature of the adsorption process (Fig. 7c). Regarding geometric structures, the effect of the interlayer spacing and the diameter of the CNTs on H_2 storage efficiency was determined. The simulations showed that H_2 storage efficiency was relatively low when the interlayer spacing was small, such that H_2 molecules adsorbed at graphene edges because they could not enter the structures effectively (Fig. 7d). However, an increase in CNT diameter led to an increase in the CNTs' accessible surface area and thus an increase in the volume of H_2 adsorbed.

Subsequently, Dimitrakakis et al.[70] used grand canonical Monte Carlo (GCMC) simulations to investigate how to improve the H_2 storage capacity of pillared graphene. Various combinations of CNTs of different curvatures, inter-tube distances, and graphene-sheet interlayer distances were tested to achieve the best possible H_2 adsorption. Their analysis showed that, across all combinations of CNTs and graphene, the gravimetric adsorption capacities for H_2 were consistently lower than those of the original structures (Fig. 7e). This was attributed to the substantial increase in the overall weight of CNT/graphene nanocomposites that resulted from the insertion of CNT bundles. However, the volumetric adsorption of H_2, which is dependent only on the number of H_2 molecules adsorbed, substantially improved. For instance, utilization of SWCNTs with an inter-tube distance of 1.5 nm and graphene sheets with an interlayer distance of 1.2 nm resulted in a substantial (25%)

enhancement in volumetric H_2 adsorption at ambient temperature, compared with that of graphene or CNTs alone (Fig. 7f). Furthermore, the incorporation of Li ions (Li^+) as a dopant resulted in improvements in both gravimetric and volumetric H_2 adsorption. This was attributed to an increase in the binding energy per mole of H_2 of the Li^+-doped CNT/graphene nanocomposite (~14.2 kJ mol^{-1}) compared with that of the undoped CNT/graphene composite (~1.38 kJ mol^{-1}).

The study by Larijani et al.[77] has adopted further modifications of carbon nanotubes (CNTs) through the decoration with nanoparticles of transition metal oxides. The incorporation of these transition metal oxides can enhance hydrogen storage due to the active catalytic role of the metals. A comparative evaluation involving TiO_2, Pd, and PdO nanoparticles within CNTs has revealed that the hydrogen storage performance follows the ascending order indicated below: PdO < Pd < TiO_2. The relatively inferior performance of PdO, compared to Pd, is hypothesized to result from the presence of a thick PdO layer that suppresses the catalytic activity of Pd with hydrogen molecules. In contrast, in comparison to TiO_2-incorporated CNTs, it was observed that the robust interaction between Ti atoms on the anatase (101) surface promotes the electrical adsorption of hydrogen molecules. However, it should be noted that the effective dispersion of transition metal oxides can significantly impact H_2 uptake, which represents a crucial area for future investigation.

CO_2 adsorption. The capability of 2D materials to perform CO_2 capture has been investigated with the use of LDHs, as they possess attractive properties: a low energy penalty for regeneration, fast adsorption–desorption kinetics, and stable performance under humid conditions[78–81]. Nevertheless, the applicability of LDHs in CO_2 capture remains limited by their low CO_2 adsorption capacity. Therefore, the development of LDH-based composites has involved the incorporation of several adsorbents with large surface areas, such as alumina (Al_2O_3), zeolites, and carbon-based materials[82–84].

For example, the incorporation of oxidized MWCNTs into an LDH led to LDH/MWCNT composites with enhanced water solubilities due to the presence of carboxylate sites on oxidized MWCNTs[42]. It has also been observed that the incorporation of a nanostructured network, i.e., oxidized MWCNTs, into an LDH has three main effects. First, it increases the accessible surface area with respect to the LDH, resulting in a systematic increase in gas adsorption capacity. Specifically, although there is no apparent change in the micropore volume, it results in a decrease in the pore size distribution (Fig. 8a). Second, it introduces defects into the LDH structure due to MWCNTs modifying the nucleation conditions or inducing curvatures. This was verified by peak broadening in the XRD pattern (calculated from the Scherrer equation) observed with an increase in the concentration of oxidized MWCNTs (Fig. 8b). Third, it mitigates the sintering effect during calcination, thereby minimizing the collapse of LDH structures and enhancing their stability. This is due to the ionic interaction between oxidized MWCNTs and LDH nanosheets, which are negatively and positively charged, respectively. These three effects account for the CO_2 adsorption increasing by 170% (at 0.2 bar and 300 °C) as the oxidized MWCNT content was increased from 20 to 70 wt% (Fig. 8c).

LDH/oxidized MWCNT structures have also been investigated in other studies. For instance, Wang et al.[39] prepared two different types of LDH/oxidized MWCNT nanocomposites through an exfoliation self-assembly method and a direct co-precipitation method. Exfoliation self-assembly involved the assembly of exfoliated LDH nanosheets and oxidized MWCNTs to form LDH–NO_3–NS/OCNT, whereas direct co-precipitation involved an in situ reaction between the raw materials for LDH nanosheet preparation and dispersed oxidized MWCNTs to form LDH–NO_3/OCNT and LDH–CO_3/OCNT, respectively. The enhanced dispersion and stabilization of LDH nanosheets achieved via the direct co-precipitation method resulted in LDH/oxidized MWCNT nanocomposites with better CO_2 capture performance than those prepared by the exfoliation self-assembly method. Thus, under the same measurement conditions (1 bar CO_2 and 200 °C), LDH–CO_3/OCNT demonstrated a higher CO_2 adsorption capacity than LDH–NO_3–NS/OCNT (Fig. 8d) due to the optimized ratio of LDH and OCNT in the former nanocomposite. It is postulated that the optimized quantity of LDH and OCNT results in geometric compatibility, which is expected to promote heterogeneous nucleation. This, in turn, leads to the creation of additional active sites for CO_2 adsorption[85–87]. Furthermore, the recyclability of LDH–CO_3/OCNT in CO_2 capture, which was verified through repetitive runs for 22 cycles, resulted in a regenerability of ~80%, indicating its feasibility for use in rapid adsorption–desorption cycling for CO_2 capture. Furthermore, additional tuning of gas adsorption performance was conducted by Bhatta et al.[40] through the addition of alkali metals (e.g., potassium carbonate), which achieved a relatively constant working capacity of 0.81 mmol g^{-1} at 300–400 °C after operating for 10 cycles at ambient pressure.

Additional investigations on the application of MWCNT-GO as a mixed substrate for deposition onto an LDH support have been performed. Macro et al.[41] found that GO/MWCNT (1:1)-LDH nanocomposites exhibited higher accessible surface areas (103.5 $m^2 g^{-1}$) than MWCNT-LDH (77.7 $m^2 g^{-1}$) and GO-LDH (84.9 $m^2 g^{-1}$). This was attributed to the increased exfoliation of GO layers in the GO/MWCNT mixed substrate, which resulted in increased structural porosity. Furthermore, the XRD pattern of the LDH support revealed that LDH in a GO/MWCNT (1:1)-LDH nanocomposite had a smaller platelet thickness (13.7 nm) than LDH alone (22.8 nm), thus resulting in an increase in the active sites available for CO_2 adsorption in the nanocomposite. This resulted in a 172% enhancement in the CO_2 adsorption capacity of the GO/MWCNT (1:1)-LDH nanocomposite compared with that of LDH alone (Fig. 8e). Furthermore, the CO_2 adsorption capacity of the GO/MWCNT (1:1)-LDH nanocomposite remained at 96% of its original capacity throughout a 20-cycle adsorption–desorption measurement.

The applicability of 1D–2D nanocomposites beyond those based on CNTs has been examined in various studies. For instance, 1D materials such as Al_2O_3 nanorods possess the advantages of good hydrothermal stability and low production cost. However, these materials have smaller accessible surface areas and lower thermal conductivities than silica and MOFs. Therefore, improvements have been made to Al_2O_3–2D nanocomposites to enhance their capacity for CO_2 capture. Bhowmik et al.[88] impregnated poly(ethyleneimine) (PEI) into a γ-Al_2O_3 nanorod/rGO (γ-Al_2O_3/rGO) nanocomposite that possessed well-defined mesopores, resulting from the entanglement of γ-Al_2O_3 nanorods with rGO. The γ-Al_2O_3/rGO nanocomposite had a 34% greater BET surface area than that of γ-Al_2O_3 nanorods, implying its potential utility as a substrate for PEI impregnation to design an amine-appended CO_2 capturing adsorbent. An optimization process revealed that the impregnation of 6.49 mmol g^{-1} of amines onto γ-Al_2O_3/rGO nanocomposite resulted in the highest CO_2 adsorption capacity (1.36 mmol g^{-1}). Further increases in the amine loading, however, led to blockage of pores by amine molecules and thus decreases in the CO_2 adsorption capacity. Furthermore, an increase in thermal conductivity (from 0.5 to 1.3 W m^{-1} K^{-1}) through the incorporation of rGO resulted in a minimization of the local overheating effect that can occur during adsorption (as adsorption is an exothermic process). This helped to prevent the degradation of PEI, which is critical for repetitive adsorption–desorption cycling. This is consistent with the reported data, which show that the volume of CO_2 adsorbed was relatively constant (within 6.3% of that adsorbed

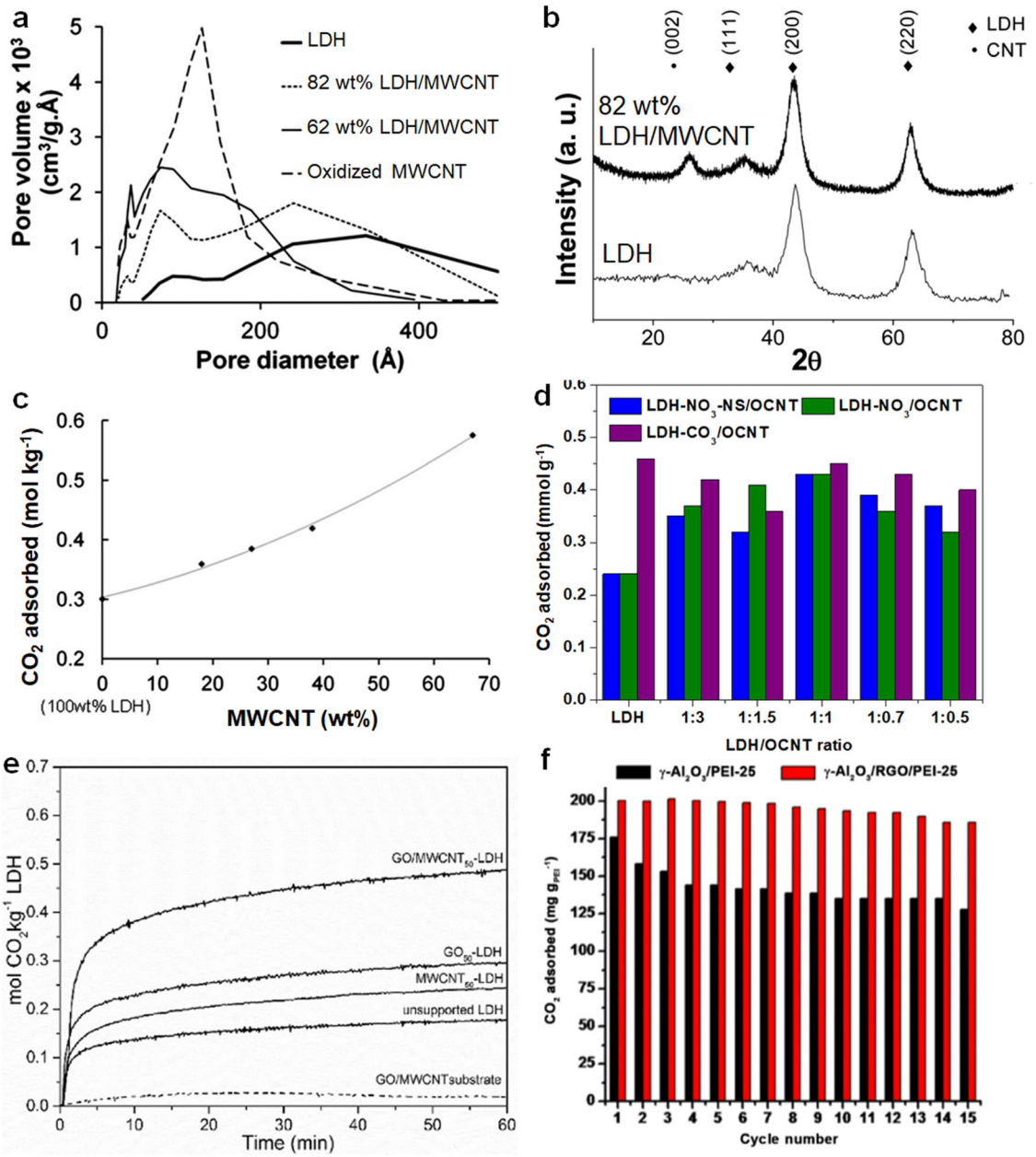

Fig. 8 CO_2 capture in 1D–2D nanocomposites. a Pore size distribution of LDH, MWCNT, and LDH/MWCNT nanocomposites. The calculation was performed on the desorption branch using the Barrett, Joyner, and Halenda method. **b** XRD pattern of LDH and LDH/MWCNT nanocomposites. The scanning is conducted at ambient temperature via Cu Kα diffractor ($\lambda = 0.154$ nm). **c** CO_2 adsorption per unit mass of LDH and LDH/MWCNT nanocomposites as a function of MWCNT content at 300 °C and 0.2 bar of CO_2. **a**–**c** are reprinted with permission from ref. [42], Copyright 2012 The Royal Society of Chemistry. **d** Comparison of CO_2 adsorption capacity of LDH:OCNT nanocomposites with variation of the LDH:OCNT ratio at 200 °C and 1 bar. The data in this graph were extracted from ref. [39]. **e** Comparison of CO_2 adsorption kinetics (for the first cycle) of LDH with GO:MWCNT (1:1) substrate at 300 °C and 0.2 bar. **e** is reprinted with permission from ref. [41], Copyright 2017 Elsevier. **f** Measurement of repetitive CO_2 adsorption–desorption cycling of γ-Al_2O_3/RGO/PEI-25 and γ-Al_2O_3/PEI-25 at 75 °C and 0.15 bar. **f** is reprinted with permission from ref. [88], Copyright 2016 Wiley-VCH Verlag GmbH & Co.

in the first cycle) in a 15-cycle operation (Fig. 8f). Xia et al. reported carbon nitride nanorod array (CNNA)/rGO as another type of 1D–2D nanocomposite that exhibited potential applications in CO_2 capture[89]. In particular, CNNA/rGO nanocomposites had much greater CO_2 adsorption capacities than their individual precursors, as verified by the higher $-Q_{st}$ of CNNA/rGO nanocomposites (55 kJ mol^{-1}) than those of CNNA (15 kJ mol^{-1}) or rGO (18 kJ mol^{-1}). This may be attributable to changes in the electronic environment and charge redistribution resulting from the presence of delocalized electron clouds in rGO, which is in sp^2 hybridized form.

3D–2D nanocomposites

In comparison with the research on 0D–2D nanocomposites and 1D–2D nanocomposites, the research on 3D–2D structures has been more extensive. Among 3D nanomaterials, MOFs are the most promising candidates due to their large structural porosities and readily tunable structures. In particular, copper (Cu)-based MOFs have proven highly favorable for gas adsorption due to their abundance of open metal sites[90]. The spaces between nanosheets and nanoparticles play an important role in enhancing the gas adsorption performance of 3D–2D nanocomposites. Thus, in this

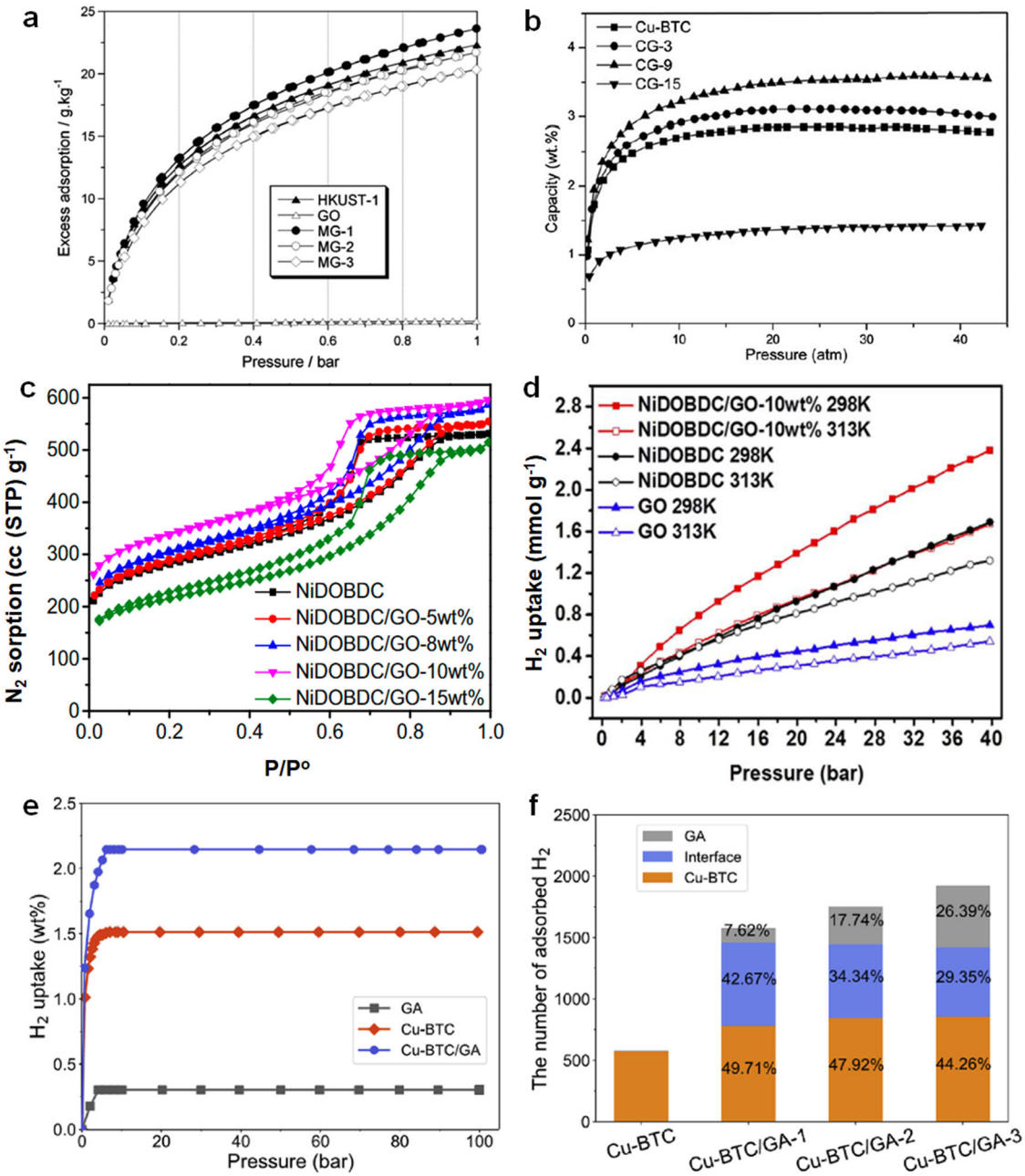

Fig. 9 Hydrogen storage in 3D-2D nanocomposites. a H_2 adsorption of HKUST-1, GO and HKUST-1/GO nanocomposites (MG-1, MG-2, and MG-3) at 77 K. **a** is reprinted with permission from ref. [91], Copyright 2011 Elsevier. **b** H_2 adsorption (77 K) of HKUST-1, GO, and HKUST-1/GO nanocomposites (CG-3, CG-9, and CG-15). **b** is reprinted with permission from ref. [30], Copyright 2013 Royal Society of Chemistry. **c** N_2 physisorption (77 K) of NiDOBDC and NiDOBDC/GO nanocomposites. **d** H_2 adsorption isotherm of NiDOBDC, GO, and NiDOBDC/GO nanocomposites up to 40 bar at 25 °C and up to 40 bar at 40 °C. **c**, **d** are reprinted with permission from ref. [43], Copyright 2018 Elsevier. **e** Comparison of measured and simulated H_2 adsorption isotherm of GA (graphene aerogel), Cu-BTC, and Cu-BTC/GA nanocomposites at 77 K. **f** Number of H_2 molecules adsorbed by Cu-BTC and Cu-BTC/GA-based nanocomposites. Cu-BTC/GA-*n* (where $n = 1$, 2, or 3, and denotes the number of GO layers in Cu-BTC/GA), based on the measurement conducted at 100 bar and 77 K. **e**, **f** are reprinted with permission from ref. [94], Copyright 2011 Elsevier.

section, the applications of 3D–2D nanocomposites in H_2 storage and CO_2 capture are discussed.

H_2 adsorption and storage. Petit et al. explored the applicability of Cu-based MOFs combined with GO nanocomposites (i.e., HKUST-1/GO) for H_2 adsorption and storage[91]. HKUST-1/GO is a nanocomposite with an enhanced interaction between Cu dimers in HKUST-1 and epoxy groups in GO. This synergistic effect was verified by the increasing H_2 adsorption of HKUST-1/GO nanocomposites with increasing GO contents (Fig. 9a) being consistent with their BET surface areas. This was due to the improved dispersion of 2D GO layers during the fabrication of HKUST-1/GO nanocomposites. Similar behavior was reported by Liu et al.[30], who found that an HKUST-1/GO nanocomposite that had a high H_2 adsorption capacity (CG-9) also had a high BET surface area (Fig. 9b).

Another MOF/rGO nanocomposite that was investigated was a zirconium (Zr)–MOF/rGO nanocomposite. Similarly, this

nanocomposite was formed through the in situ growth of a Zr–MOF with rGO nanosheets[92] and had a 32% greater accessible surface area than that of pristine Zr–MOF. This led to the (Zr)–MOF/rGO nanocomposite having an H_2 storage capacity (at 77 K and 1 bar) of 1.8 wt%, which was greater than that of Zr–MOF (1.4 wt%). However, additional optimization of the ratio of Zr–MOF and rGO was required due to the potential presence of both rGO stacks and Zr–MOF/rGO nanocomposites during synthesis. Li et al.[43] also observed such behavior in the synthesis and development of NiDOBDC/GO nanocomposites. In the optimization process, a drastic decrease in BET surface areas was observed when the loading of GO increased beyond 10 wt% (Fig. 9c). Thus, the H_2 storage potential of NiDOBDC/GO-10% was investigated, revealing that it had a 27% greater BET surface area and a 50% greater H_2 adsorption at 25 °C and 40 bar (Fig. 9d) than the NiDOBDC framework.

The incorporation of functionalized MOFs toward the creation of MOF/GO nanocomposites has also been explored. Dasbaz et al.[93] intercalated amine-functionalized copper terephthalate (Cu–BDC–NH_2) MOFs with GO for potential applications in H_2 storage. The additional space formed in the Cu-BDC-NH_2/GO nanocomposite increased the accessibility of its sites for H_2 storage. This translated into a 42% improvement in H_2 storage capacity under the same measurement conditions (77 K and 40 bar). It was postulated that GO served as a modulation agent to extend the space between metal nodes in the Cu-BDC framework, thereby increasing the accessible surface area.

The applicability of 3D–2D nanocomposites in H_2 storage applications has also been examined through simulation and experimental studies. For example, Ren et al.[94] used experimental and simulation (GCMC) studies to examine H_2 adsorption in developed nanocomposites and pristine structures. First, they found a distinct difference in experimental and simulation results in terms of overall H_2 adsorption capacities. For instance, an H_2 adsorption capacity of 2.15 wt% was exhibited by an HKUST-1/graphene aerogel (Fig. 9e) at 77 K and 100 bar. In contrast, the H_2 adsorption capacity of HKUST-1/graphene aerogel in simulations ranged from 7 to 9 wt%, depending on the number of GO layers available in the nanocomposites. This high H_2 adsorption capacity was attributed to the perfect crystalline structures of the simulated HKUST-1/graphene aerogel resulting in large surface areas and pore volumes. Furthermore, in the simulation study, a HKUST-1/graphene aerogel based on a single-layer graphene aerogel had a higher H_2 adsorption capacity than other frameworks. This was potentially due to its accessible surface area decreasing as the number of graphene aerogel layers increased. Nevertheless, according to the calculated number of H_2 molecules adsorbed per unit volume, an HKUST-1/graphene aerogel with the greatest number of graphene aerogel layers had the most effective structure for H_2 adsorption (Fig. 9f). This may be attributable to an increased density of gas storage sites for H_2 adsorption, resulting in an increase in the number of H_2 molecules adsorbed in the interface between HKUST-1 and the graphene aerogel.

MXene, a carbide-based material, has been explored for its potential application in H_2 storage. This has been achieved by incorporating nanoparticles into MXene. In a study by Hang et al.[95], perovskite hydride ($NaMgH_3$) was introduced into the layers of 2D MXene. It has been observed that the presence of lamellar structures within the 2D MXene demonstrates the feasibility of achieving reversible hydrogen storage capacity (approximately 4.6 wt%) after five cycles. This approach has aided in enhancing the role of $NaMgH_3$ as a hydrogen storage material. This is particularly important as $NaMgH_3$ is suited for H_2 storage through a two-step de/re-hydrogenation process; however, its limited cycling stability and sluggish kinetics have restricted its practical applicability. Therefore, the distinctive 2D MXene layers have the capacity to evenly disperse the agglomerated $NaMgH_3$ particles, thus reducing the activation energy required for the hydrogen storage process. Similar analyses are corroborated by other nanocomposites utilizing the capabilities of 2D materials to minimize particle agglomeration, as reported in other sections[43].

CO_2 adsorption. Evaluations of 3D–2D nanocomposites for potential applications in CO_2 adsorption have been performed by several groups of researchers. Similar to studies of H_2 adsorption, one of the 3D–2D nanocomposites that have been studied thoroughly is composed of HKUST-1 and GO[30,91,96,97]. Moreover, Zhao et al.[98] compared two types of HKUST-1/GO nanocomposites, containing either GO or aminated GO, at the same loading (10 wt% GO). An optimization showed that as the proportion of amine attached to the porous GO framework increased, the CO_2 adsorption capacity increased under all conditions (0 and 23 °C). This may be attributable to an increase in the number of gas storage sites through the creation of additional micropores. This was evident by comparing MOF/GO-U3 with a MOF framework. That is, compared with the MOF, the increased BET surface area (53%) and proportion of micropores (51%) in the MOF/GO-U3 framework translated into a 100% increase in CO_2 adsorption capacity (Fig. 10a). Furthermore, an increase in the proportion of pendant amine groups resulted in a decrease in the overall micropore size, allowing preferential adsorption of CO_2 into the available gas storage sites.

The application of UiO-66/GO nanocomposites for gas separation has been studied by various groups. Cao et al.[99] explored UiO-66/GO nanocomposites with various loadings and found that the optimal configuration (UiO-66/GO-5) achieved the optimal porosity properties with reference to UiO-66 or GO. It was found that the additional pores can be formed in UiO-66/GO nanocomposites, and the optimized UiO-66/G-5 sample exhibited the CO_2 adsorption of ~3.37 mmol g^{-1} at 25 °C and 1 bar which is 49% greater than that of UiO-66 (Fig. 10b). Furthermore, the adsorbents could be regenerated for repetitive adsorption–desorption cycling, allowing six-cycle operation.

Incorporation of other 3D–2D frameworks has also been investigated. Kamal et al.[21] explored nanocomposites of Mg-MOF-74/GO and Mg-MOF-74/CNT for potential applications in CO_2 capture. As expected, with the appropriate tuning and optimization of the overall structure, increases in accessible surface areas and pore volume (Fig. 10c) were achieved, resulting in improvements in CO_2 adsorption capacities of 18% and 23% for Mg–MOF-74/CNT and Mg–MOF-74/GO, respectively, at 25 °C and 1 bar. Tests of material stability by 18 months of aging under inert conditions indicated that there were no substantial changes in overall crystallinity and structural porosity. However, as Mg–MOF-74 possessed poor hydrolytic stability due to the presence of unsaturated open metal sites[90,100], supplementary tests under repetitive adsorption–desorption cycling in humid conditions are required to determine its applicability to practical CO_2 capture processes. In this regard, the MOF-74 analog NiDOBDC (Ni-MOF-74) is more suited for CO_2 adsorption due to its being more stable than Mg–MOF-74. Li et al. have found that the CO_2 adsorption capacity of a Ni-MOF-74/GO-10% nanocomposite (4.58 mmol g^{-1}) is somewhat higher than that of Ni–MOF-74 (4.03 mmol g^{-1}) and GO (0.34 mmol g^{-1}) under the same conditions (25 °C and 1 bar)[43,44]. This is consistent with the surface areas of 3D–2D nanocomposites being more accessible than those of Ni–MOF-74 (Fig. 10d).

SUMMARY AND ANALYSIS OF H_2 AND CO_2 ADSORPTION DATA

The H_2 storage and CO_2 capacities of mixed-dimensional nanocomposites are summarized in Supplementary Table 2. The predicted properties of hypothetical mixed-dimensional nanocomposites are shown in Supplementary Table 3. In terms of CO_2 capture performance, there is no simple structure–property correlation, as many chemical and physical properties can

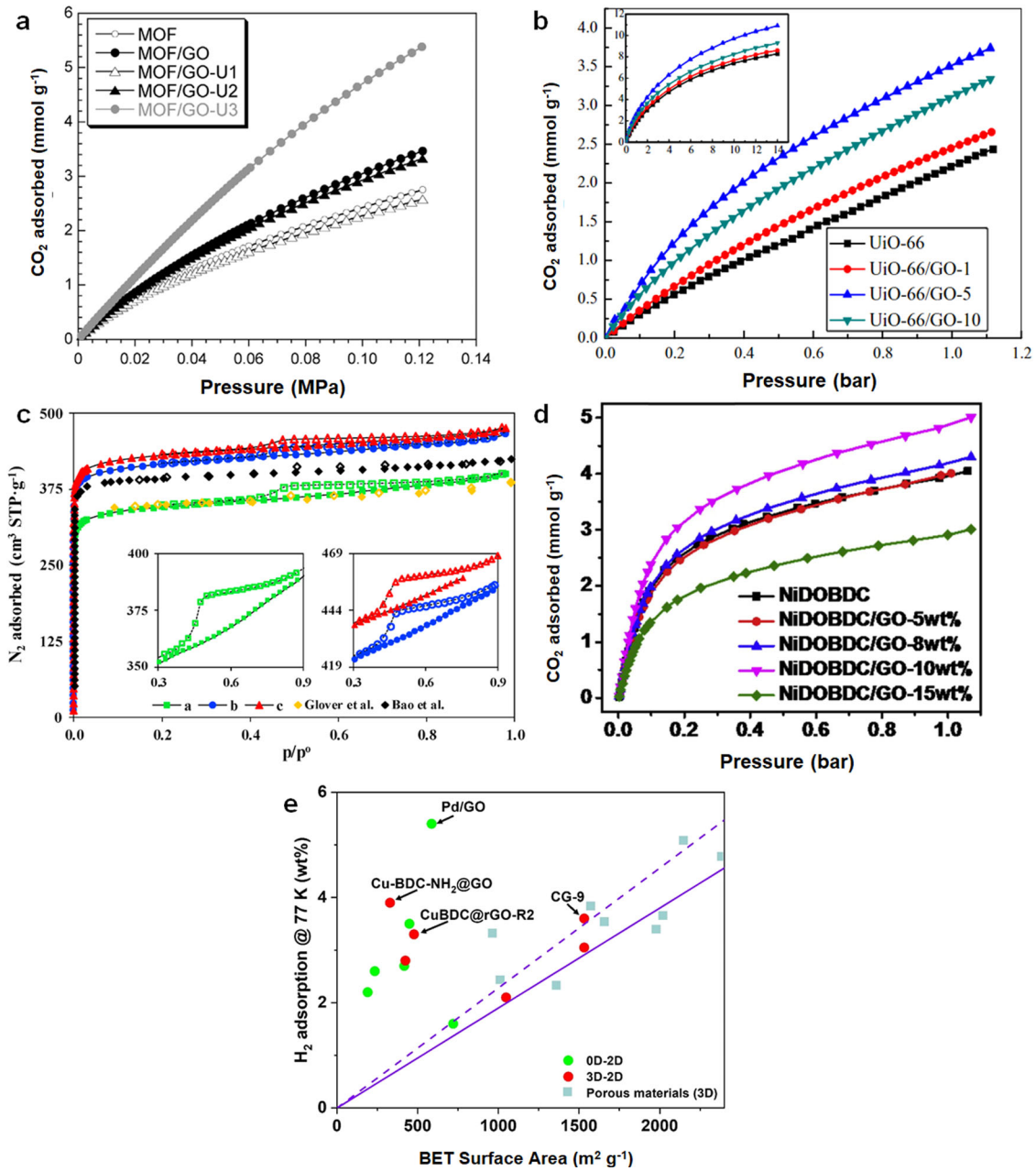

Fig. 10 CO_2 capture in 3D-2D nanocomposites. a CO_2 adsorption isotherm at 23 °C for HKUST-1, HKUST-1/GO nanocomposites and HKUST-1/aminated GO nanocomposites (MOF/GO-U1, MOF/GO-U2, MOF/GO-U3). **a** is reprinted with permission from ref. [98], Copyright 2014 Elsevier. **b** CO_2 adsorption at 25 °C of UiO-66 and UiO-66/GO nanocomposites. **b** is reprinted with permission from ref. [99], Copyright 2015 Elsevier. **c** N_2 physisorption isotherm (77 K) of Mg-MOF-74 [a]; Mg-MOF-74@CNT [b] and Mg-MOF-74@GO [c]. **c** is reprinted with permission from ref. [21], Copyright 2021 Elsevier. **d** CO_2 adsorption at 25 °C of NiDOBDC and NiDOBDC/GO nanocomposites. **d** is reprinted with permission from ref. [43], Copyright 2018 Elsevier. **e** H_2 adsorption of selected mixed-dimensional (0D–2D and 3D–2D) nanocomposite, measured at 77 K and >20 bar. The data were extracted from Supplementary Table 2, and the data of homogeneous 3D porous materials were obtained from a study on MOFs[101,102]. The solid reference line was obtained from the plot of excess gravimetric adsorption capacity vs. surface area of porous carbon, and the dashed line indicates the estimated upper limit of H_2 adsorption (where the H_2 is adsorbed into a monolayer and has the density of liquid-phase H_2)[105].

simultaneously affect this performance. However, for H_2 storage at a cryogenic temperature, surface area is the dominant factor affecting performance. Figure 10e shows a summary plot illustrating a correlation between H_2 storage capacity (77 K and >20 bar) and BET surface area. Homogeneous porous materials (e.g., MOFs) are included with mixed-dimensional nanocomposites[101,102]. It can be observed that mixed-dimensional nanocomposites are superior to homogeneous porous materials as adsorbents. This is mainly because of the creation of additional pore spaces in mixed-dimensional nanocomposites, which is evidenced by increases in BET surface areas as compared to homogeneous porous materials. It is worth noting that, in the case of MOFs, while the judicious selection of building blocks such as ligands with elongated strut can indeed elevate the surface area, it can also result in MOFs with poor hydrolytic stabilities, hence limiting their practical applications[103,104]. Furthermore, it is clearly evident that many of the nanocomposites have overcome reported theoretical limitations for homogeneous porous

materials. To be specific, in Fig. 10e, the solid line represents experimentally measured H_2 adsorption capacities of porous carbon materials, whereas the dashed line represents the theoretical maximum H_2 adsorption capacity[105]. Note that the dashed line is drawn under the assumption that the density of liquid H_2 cannot be overcome by forming a multilayer of H_2 molecules on the surface of porous materials. Similar trends have been found for MOFs, zeolites, and Prussian blue analogs[33,106]. The storage performance of nanocomposites which are located far above the dashed line, highlights the advantages of hierarchical structures constructed by components with two different characteristics. It is important to emphasize that there exists no correlation between CO_2 adsorption and BET surface area, as CO_2 adsorption is significantly impacted by chemical properties.

DISCUSSION

This review showcases recent investigations of mixed-dimensional nanocomposites for applications in H_2 adsorption and CO_2 capture processes. It illustrates that developing mixed-dimensional nanocomposites may reveal new avenues for the design of high-performance nanoporous adsorbents based on synergistic interactions between materials of different dimensions. An advantage of developing mixed-dimensional nanocomposites lies in their inherent simplicity. In contrast to the intricate process of developing entirely new materials, which demands substantial effort, enhancing gas adsorption capacity can be accomplished by the mere physical blending of two established materials. Moreover, this strategy holds the potential for extensive expansion to encompass numerous plausible combinations. Nevertheless, effective utilization of mixed-dimensional nanocomposite adsorbents in real-life applications will require substantial further investigations.

Most studies have heavily relied on the measurement of pure-component gas adsorption isotherms. However, analogous with studies of greenhouse gas capture, such as pre- and post-combustion carbon capture, and studies of sulfur hexafluoride recovery, measurement of the $-Q_{st}$ of a specific adsorbate is critical for gas adsorption and storage determination, as it illustrates the energy penalty for adsorbents' regeneration[90,107]. The calculations of $-Q_{st}$ can be performed mathematically using the Clausius–Clapeyron equation, based on the gas adsorption isotherms measured at least two different temperatures separated by 10 °C[1,108,109]. A more accurate method reported is a calorimetric measurement despite such measurement being challenging to conduct experimentally[2].

In addition, it is also critical to measure the gas adsorption kinetics of mixed-dimensional nanocomposites in the context of gas adsorption and storage processes, as such kinetics dictate the overall processing rate of an adsorbent in adsorption–desorption cycling[110]. New pore spaces can be formed in mixed-dimensional nanocomposites, which can be captured by the measurements of pore size distribution and BET surface area. If the developed adsorbents are present in a tight-pore configuration[111], the diffusions of gas molecules can potentially be limited, leading to poor adsorption–desorption kinetics. The adsorption kinetics analysis can be typically conducted through either (1) measurement of the pressure decrease over time at a specific dosing pressure; or (2) breakthrough measurement, which can showcase the mass transfer limitation in a gas adsorption at a dynamic flow condition[112,113].

For practical applications, the long-term stability of mixed-dimensional nanocomposites should be validated under realistic conditions. For example, the nanoarchitecture constructed from materials of different dimensions may collapse upon exposure to repetitive adsorption–desorption cycling under conditions relevant to practical applications. Moreover, the functionalities introduced into nanocomposites may be gradually denatured over time. As this field is in its infancy, researchers have yet to explore the long-term stability of mixed-dimensional nanocomposites. This must be undertaken, as it is a highly important factor affecting the economic feasibility of gas adsorption processes.

Finally, although fundamental investigations of mixed-dimensional nanocomposites in gas adsorption and storage processes are critical, these materials must ultimately be developed in monolith forms rather than powdered forms due to the potential for large pressure decreases and inefficient heat transfer across an adsorption column[1,2]. In this regard, 2D materials can often function usefully as binders. We believe that this is an important area for future research that could realize practical applications of mixed-dimensional nanocomposites as gas adsorbents.

DATA AVAILABILITY

The availability of research data is not applicable to this review article. The relevant figures and tables are duly cited in the texts.

CODE AVAILABILITY

The availability of computational code is not applicable to this review article.

Received: 10 April 2023; Accepted: 28 August 2023;
Published online: 06 September 2023

REFERENCES

1. Chuah, C. Y., Lee, H. & Bae, T.-H. Recent advances of nanoporous adsorbents for light hydrocarbon (C_1–C_3) separation. *Chem. Eng. J.* **430**, 132654 (2022).
2. Chuah, C. Y., Lee, Y. & Bae, T.-H. Potential of adsorbents and membranes for SF_6 capture and recovery: a review. *Chem. Eng. J.* **404**, 126577 (2021).
3. Sumida, K. et al. Carbon dioxide capture in metal–organic frameworks. *Chem. Rev.* **112**, 724–781 (2012).
4. Chuah, C. Y. et al. Harnessing filler materials for enhancing biogas separation membranes. *Chem. Rev.* **118**, 8655–8769 (2018).
5. Lee, Y., Chuah, C. Y., Lee, J. & Bae, T.-H. Effective functionalization of porous polymer fillers to enhance CO_2/N_2 separation performance of mixed-matrix membranes. *J. Membr. Sci.* **647**, 120309 (2022).
6. Saleh, T. A. Nanomaterials and hybrid nanocomposites for CO_2 capture and utilization: environmental and energy sustainability. *RSC Adv.* **12**, 23869–23888 (2022).
7. Saleh, T. A. & Fadillah, G. Efficient detection of CO_2 by nanocomposites: environmental and energy technologies. *Trends Environ. Anal. Chem.* **32**, e00142 (2021).
8. Saleh, T. A. Organic–inorganic hybrid nanocomposites for the photoreduction of CO_2: environment and energy technologies. *Bull. Mater. Sci.* **45**, 222 (2022).
9. Fadillah, G. & Saleh, T. A. Advances in mesoporous material for adsorption and photoconversion of CO_2 in environmental pollution: Clean environment and clean energy. *Sustain. Chem. Pharm.* **29**, 100812 (2022).
10. Chuah, C. Y., Kim, K., Lee, J., Koh, D.-Y. & Bae, T.-H. CO_2 absorption using membrane contactors: Recent progress and future perspective. *Ind. Eng. Chem. Res.* **59**, 6773–6794 (2019).
11. Hwang, H. T. & Varma, A. Hydrogen storage for fuel cell vehicles. *Curr. Opin. Chem. Eng.* **5**, 42–48 (2014).
12. Li, W. *Advanced Gas Separation via Combined Use of Carbon Nanomaterials And Microporous Materials*. Doctor of Philosophy thesis. (Nanyang Technological University, 2019).
13. Feng, C. et al. Key technology and application analysis of zeolite adsorption for energy storage and heat-mass transfer process: a review. *Renew. Sust. Energ. Rev.* **144**, 110954 (2021).
14. Yang, Y., Chuah, C. Y., Gong, H. & Bae, T.-H. Robust microporous organic copolymers containing triphenylamine for high pressure CO_2 capture application. *J. CO2 Util.* **19**, 214–220 (2017).
15. Serna-Guerrero, R., Da'na, E. & Sayari, A. New insights into the interactions of CO_2 with amine-functionalized silica. *Ind. Eng. Chem. Res.* **47**, 9406–9412 (2008).
16. Yang, Y. et al. Sub-Ångström-level engineering of ultramicroporous carbons for enhanced sulfur hexafluoride capture. *Carbon* **155**, 56–64 (2019).
17. Chuah, C. Y. & Laziz, A. M. Recent progress in synthesis and application of activated carbon for CO_2 capture. *C* **8**, 29 (2022).

18. Yang, Y., Chuah, C. Y. & Bae, T.-H. Polyamine-appended porous organic polymers for efficient post-combustion CO_2 capture. *Chem. Eng. J.* **358**, 1227–1234 (2019).
19. McDonald, T. M. et al. Capture of carbon dioxide from air and flue gas in the alkylamine-appended metal–organic framework mmen-Mg_2(dobpdc). *J. Am. Chem. Soc.* **134**, 7056–7065 (2012).
20. Petit, C. & Bandosz, T. J. MOF–graphite oxide composites: combining the uniqueness of graphene layers and metal–organic frameworks. *Adv. Mater.* **21**, 4753–4757 (2009).
21. Kamal, K., Grekov, D. I., Shariff, A. M., Bustam, M. A. & Pré, P. Improving textural properties of magnesium-based metal-organic framework for gas adsorption by carbon doping. *Micropor. Mesopor. Mater.* **323**, 111246 (2021).
22. Kumar, R., Jayaramulu, K., Maji, T. K. & Rao, C. Hybrid nanocomposites of ZIF-8 with graphene oxide exhibiting tunable morphology, significant CO_2 uptake and other novel properties. *Chem. Commun.* **49**, 4947–4949 (2013).
23. Cote, L. J. et al. Graphene oxide as surfactant sheets. *Pure Appl. Chem.* **83**, 95–110 (2010).
24. Sui, Z.-Y., Cui, Y., Zhu, J.-H. & Han, B.-H. Preparation of three-dimensional graphene oxide–polyethylenimine porous materials as dye and gas adsorbents. *ACS Appl. Mater. Interface* **5**, 9172–9179 (2013).
25. Kim, T. K. et al. Three-dimensional pillared metallomacrocycle–graphene frameworks with tunable micro-and mesoporosity. *J. Mater. Chem. A* **1**, 8432–8437 (2013).
26. Kim, B. H. et al. Thermally modulated multilayered graphene oxide for hydrogen storage. *Phys. Chem. Chem. Phys.* **14**, 1480–1484 (2012).
27. Chowdhury, S. & Balasubramanian, R. Highly efficient, rapid and selective CO_2 capture by thermally treated graphene nanosheets. *J. CO2 Util.* **13**, 50–60 (2016).
28. dos Santos, T. C. & Ronconi, C. M. Self-assembled 3D mesoporous graphene oxides (MEGOs) as adsorbents and recyclable solids for CO_2 and CH_4 capture. *J. CO2 Util.* **20**, 292–300 (2017).
29. Ma, M., Li, H., Xiong, Y. & Dong, F. Rational design, synthesis, and application of silica/graphene-based nanocomposite: A review. *Mater. Des.* **198**, 109367 (2021).
30. Liu, S. et al. Nanosized Cu-MOFs induced by graphene oxide and enhanced gas storage capacity. *Energy Environ. Sci.* **6**, 818–823 (2013).
31. Singh, R. S. CO_2 capture by metal-decorated silicon carbide nanotubes. *Silicon* **15**, 4501–4511 (2023).
32. Chen, Z., Kirlikovali, K. O., Idrees, K. B., Wasson, M. C. & Farha, O. K. Porous materials for hydrogen storage. *Chem* **8**, 693–716 (2022).
33. Morris, R. E. & Wheatley, P. S. Gas storage in nanoporous materials. *Angew. Chem. Int. Ed.* **47**, 4966–4981 (2008).
34. Zhou, C., Szpunar, J. A. & Cui, X. Synthesis of Ni/graphene nanocomposite for hydrogen storage. *ACS Appl. Mater. Interface* **8**, 15232–15241 (2016).
35. Huang, C.-C. et al. Hydrogen storage in graphene decorated with Pd and Pt nano-particles using an electroless deposition technique. *Sep. Purif. Technol.* **82**, 210–215 (2011).
36. Aboutalebi, S. H., Aminorroaya-Yamini, S., Nevirkovets, I., Konstantinov, K. & Liu, H. K. Enhanced hydrogen storage in graphene oxide-MWCNTs composite at room temperature. *Adv. Energy Mater.* **2**, 1439–1446 (2012).
37. Verdejo, R., Lamoriniere, S., Cottam, B., Bismarck, A. & Shaffer, M. Removal of oxidation debris from multi-walled carbon nanotubes. *Chem. Commun.* **5**, 513–515 (2007).
38. Wang, Z., Shirley, M. D., Meikle, S. T., Whitby, R. L. D. & Mikhalovsky, S. V. The surface acidity of acid oxidised multi-walled carbon nanotubes and the influence of in-situ generated fulvic acids on their stability in aqueous dispersions. *Carbon* **47**, 73–79 (2009).
39. Wang, J., Huang, L., Zheng, Q., Qiao, Y. & Wang, Q. Layered double hydroxides/oxidized carbon nanotube nanocomposites for CO_2 capture. *J. Ind. Eng. Chem.* **36**, 255–262 (2016).
40. Bhatta, L. K. G. et al. Layered double hydroxides/multiwalled carbon nanotubes-based composite for high-temperature CO_2 adsorption. *Energy Fuels* **30**, 4244–4250 (2016).
41. De Marco, M. et al. Hybrid effects in graphene oxide/carbon nanotube-supported layered double hydroxides: enhancing the CO_2 sorption properties. *Carbon* **123**, 616–627 (2017).
42. Garcia-Gallastegui, A. et al. Layered double hydroxides supported on multi-walled carbon nanotubes: preparation and CO_2 adsorption characteristics. *J. Mater. Chem.* **22**, 13932–13940 (2012).
43. Li, W., Chuah, C. Y., Yang, Y. & Bae, T.-H. Nanocomposites formed by in situ growth of NiDOBDC nanoparticles on graphene oxide sheets for enhanced CO_2 and H_2 storage. *Micropor. Mesopor. Mater.* **265**, 35–42 (2018).
44. Li, W., Chuah, C. Y., Nie, L. & Bae, T.-H. Enhanced CO_2/CH_4 selectivity and mechanical strength of mixed-matrix membrane incorporated with NiDOBDC/GO composite. *J. Ind. Eng. Chem.* **74**, 118–125 (2019).
45. Kang, C. et al. Insertion of CO_2 in metal ion-doped two-dimensional covalent organic frameworks. *Proc. Natl Acad. Sci.* **120**, e2217081120 (2023).
46. Kumar, R. et al. Nanohole-structured and palladium-embedded 3D porous graphene for ultrahigh hydrogen storage and CO oxidation multifunctionalities. *ACS Nano* **9**, 7343–7351 (2015).
47. Li, Y. & Yang, R. T. Significantly enhanced hydrogen storage in metal-organic frameworks via spillover. *J. Am. Chem. Soc.* **128**, 726–727 (2006).
48. Im, J., Shin, H., Jang, H., Kim, H. & Choi, M. Maximizing the catalytic function of hydrogen spillover in platinum-encapsulated aluminosilicates with controlled nanostructures. *Nat. Commun.* **5**, 1–8 (2014).
49. Kostoglou, N. et al. Effect of Pt nanoparticle decoration on the H_2 storage performance of plasma-derived nanoporous graphene. *Carbon* **171**, 294–305 (2021).
50. Ismail, N., Madian, M. & El-Shall, M. S. Reduced graphene oxide doped with Ni/Pd nanoparticles for hydrogen storage application. *J. Ind. Eng. Chem.* **30**, 328–335 (2015).
51. Liu, Y., Zhang, Z. & Wang, T. Enhanced hydrogen storage performance of three-dimensional hierarchical porous graphene with nickel nanoparticles. *Int. J. Hydrog. Energy* **43**, 11120–11131 (2018).
52. Hudson, M. S. L. et al. Hydrogen uptake of reduced graphene oxide and graphene sheets decorated with Fe nanoclusters. *Int. J. Hydrog. Energy* **39**, 8311–8320 (2014).
53. Wang, Y. et al. Hydrogen storage in a Ni–B nanoalloy-doped three-dimensional graphene material. *Energy Environ. Sci.* **4**, 195–200 (2011).
54. Ariharan, A., Viswanathan, B. & Nandhakumar, V. Nitrogen doped graphene as potential material for hydrogen storage. *Graphene* **6**, 41–60 (2017).
55. Huang, Z. et al. Effects of iron oxide (Fe_2O_3, Fe_3O_4) on hydrogen storage properties of Mg-based composites. *J. Alloy. Compd.* **422**, 299–304 (2006).
56. Kumar, P., Singh, S., Hashmi, S. & Kim, K.-H. MXenes: emerging 2D materials for hydrogen storage. *Nano Energy* **85**, 105989 (2021).
57. Zhang, X., Tang, C. & Jiang, Q. Electric field induced enhancement of hydrogen storage capacity for Li atom decorated graphene with Stone-Wales defects. *Int. J. Hydrog. Energy* **41**, 10776–10785 (2016).
58. Luo, D., Zhang, X. & Chen, H. Stabilized Li-decoration and enhanced hydrogen storage on reduced graphene oxides. *Int. J. Hydrog. Energy* **44**, 31192–31203 (2019).
59. Hussain, T. et al. Enhancement in hydrogen storage capacities of light metal functionalized Boron–Graphdiyne nanosheets. *Carbon* **147**, 199–205 (2019).
60. Beheshti, E., Nojeh, A. & Servati, P. A first-principles study of calcium-decorated, boron-doped graphene for high capacity hydrogen storage. *Carbon* **49**, 1561–1567 (2011).
61. Eroglu, E., Aydin, S. & Şimşek, M. Effect of boron substitution on hydrogen storage in Ca/DCV graphene: a first-principle study. *Int. J. Hydrog. Energy* **44**, 27511–27528 (2019).
62. Ozturk, Z., Baykasoglu, C. & Kirca, M. Sandwiched graphene-fullerene composite: a novel 3-D nanostructured material for hydrogen storage. *Int. J. Hydrog. Energy* **41**, 6403–6411 (2016).
63. Pavagadhi, S., Tang, A. L. L., Sathishkumar, M., Loh, K. P. & Balasubramanian, R. Removal of microcystin-LR and microcystin-RR by graphene oxide: adsorption and kinetic experiments. *Water Res.* **47**, 4621–4629 (2013).
64. Chowdhury, S. & Balasubramanian, R. Recent advances in the use of graphene-family nanoadsorbents for removal of toxic pollutants from wastewater. *Adv. Colloid Interface Sci.* **204**, 35–56 (2014).
65. Chowdhury, S., Parshetti, G. K. & Balasubramanian, R. Post-combustion CO_2 capture using mesoporous TiO_2/graphene oxide nanocomposites. *Chem. Eng. J.* **263**, 374–384 (2015).
66. Cai, J., Chen, J., Zeng, P., Pang, Z. & Kong, X. Molecular mechanisms of CO_2 adsorption in diamine-cross-linked graphene oxide. *Chem. Mater.* **31**, 3729–3735 (2019).
67. Yumura, T. & Yamasaki, A. Roles of water molecules in trapping carbon dioxide molecules inside the interlayer space of graphene oxides. *Phys. Chem. Chem. Phys.* **16**, 9656–9666 (2014).
68. Chen, L. et al. Selective CO_2 adsorption and H_2 storage in two porous amine-pillared graphene oxide frameworks. *J. Solid State Chem.* **279**, 120980 (2019).
69. Rodríguez-García, S. et al. Role of the structure of graphene oxide sheets on the CO_2 adsorption properties of nanocomposites based on graphene oxide and polyaniline or Fe_3O_4-nanoparticles. *ACS Sust. Chem. Eng.* **7**, 12464–12473 (2019).
70. Dimitrakakis, G. K., Tylianakis, E. & Froudakis, G. E. Pillared graphene: a new 3-D network nanostructure for enhanced hydrogen storage. *Nano Lett.* **8**, 3166–3170 (2008).
71. Yang, L. et al. Emerging dual-functional 2D transition metal oxides for carbon capture and Utilization: a review. *Fuel* **324**, 124706 (2022).
72. Kang, I. et al. Introduction to carbon nanotube and nanofiber smart materials. *Compos. B Eng.* **37**, 382–394 (2006).
73. Che, G., Lakshmi, B. B., Fisher, E. R. & Martin, C. R. Carbon nanotubule membranes for electrochemical energy storage and production. *Nature* **393**, 346–349 (1998).

74. Li, J. et al. Carbon nanotube sensors for gas and organic vapor detection. *Nano Lett.* **3**, 929–933 (2003).
75. McEuen, P. L., Fuhrer, M. S. & Park, H. Single-walled carbon nanotube electronics. *IEEE Trans. Nanotechnol.* **1**, 78–85 (2002).
76. Wu, C.-D., Fang, T.-H. & Lo, J.-Y. Effects of pressure, temperature, and geometric structure of pillared graphene on hydrogen storage capacity. *Int. J. Hydrog. Energy* **37**, 14211–14216 (2012).
77. Larijani, M. & Safa, S. Increase of hydrogen storage capacity of CNTs by using transition metal, metal oxide-CNT nanocomposites. *Acta Phys. Pol.* **126**, 732–735 (2014).
78. Choi, S., Drese, J. H. & Jones, C. W. Adsorbent materials for carbon dioxide capture from large anthropogenic point sources. *ChemSusChem* **2**, 796–854 (2009).
79. Hufton, J., Mayorga, S. & Sircar, S. Sorption-enhanced reaction process for hydrogen production. *AIChE J.* **45**, 248–256 (1999).
80. Ding, Y. & Alpay, E. Equilibria and kinetics of CO_2 adsorption on hydrotalcite adsorbent. *Chem. Eng. Sci.* **55**, 3461–3474 (2000).
81. Van Selow, E., Cobden, P., Verbraeken, P., Hufton, J. & Van den Brink, R. Carbon capture by sorption-enhanced water– gas shift reaction process using hydrotalcite-based material. *Ind. Eng. Chem. Res.* **48**, 4184–4193 (2009).
82. Aschenbrenner, O. et al. Adsorption of carbon dioxide on hydrotalcite-like compounds of different compositions. *Chem. Eng. Res. Des.* **89**, 1711–1721 (2011).
83. Othman, M., Rasid, N. & Fernando, W. Mg–Al hydrotalcite coating on zeolites for improved carbon dioxide adsorption. *Chem. Eng. Sci.* **61**, 1555–1560 (2006).
84. Meis, N. N., Bitter, J. H. & de Jong, K. P. On the influence and role of alkali metals on supported and unsupported activated hydrotalcites for CO_2 sorption. *Ind. Eng. Chem. Res.* **49**, 8086–8093 (2010).
85. Meis, N. N., Bitter, J. H. & de Jong, K. P. Support and size effects of activated hydrotalcites for precombustion CO_2 capture. *Ind. Eng. Chem. Res.* **49**, 1229–1235 (2010).
86. Garcia-Gallastegui, A. et al. Graphene oxide as support for layered double hydroxides: enhancing the CO_2 adsorption capacity. *Chem. Mater.* **24**, 4531–4539 (2012).
87. Wang, J. et al. Synthesis of layered double hydroxides/graphene oxide nanocomposite as a novel high-temperature CO_2 adsorbent. *J. Energy Chem.* **24**, 127–137 (2015).
88. Bhowmik, K., Chakravarty, A., Bysakh, S. & De, G. γ-Alumina nanorod/reduced graphene oxide as support for poly(ethylenimine) to capture carbon dioxide from flue gas. *Energy Technol.* **4**, 1409–1419 (2016).
89. Xia, Y. et al. Highly selective CO_2 capture and its direct photochemical conversion on ordered 2D/1D heterojunctions. *Joule* **3**, 2792–2805 (2019).
90. Chuah, C. Y., Goh, K. & Bae, T.-H. Hierarchically structured HKUST-1 nanocrystals for enhanced SF_6 capture and recovery. *J. Phys. Chem. C.* **121**, 6748–6755 (2017).
91. Petit, C., Burress, J. & Bandosz, T. J. The synthesis and characterization of copper-based metal–organic framework/graphite oxide composites. *Carbon* **49**, 563–572 (2011).
92. Musyoka, N. M. et al. Synthesis of rGO/Zr-MOF composite for hydrogen storage application. *J. Alloy. Compd.* **724**, 450–455 (2017).
93. Dastbaz, A., Karimi-Sabet, J. & Moosavian, M. A. Sonochemical synthesis of novel decorated graphene nanosheets with amine functional Cu-terephthalate MOF for hydrogen adsorption: effect of ultrasound and graphene content. *Int. J. Hydrog. Energy* **44**, 26444–26458 (2019).
94. Ren, W., Zhuang, X., Liu, Z. & Li, S. Hydrogen adsorption performance of Cu-BTC/graphene aerogel composite: A combined experimental and computational study. *Int. J. Hydrog. Energy* **46**, 13097–13105 (2021).
95. Hang, Z., Hu, Z., Xiao, X., Jiang, R. & Zhang, M. Enhancing hydrogen storage kinetics and cycling properties of $NaMgH_3$ by 2D transition metal carbide mxene Ti_3C_2. *Processes* **9**, 1690 (2021).
96. Huang, W. et al. Preparation and adsorption performance of GrO@ Cu-BTC for separation of CO_2/CH_4. *Ind. Eng. Chem. Res.* **53**, 11176–11184 (2014).
97. Zhao, Y., Seredych, M., Zhong, Q. & Bandosz, T. J. Aminated graphite oxides and their composites with copper-based metal–organic framework: in search for efficient media for CO_2 sequestration. *RSC Adv.* **3**, 9932–9941 (2013).
98. Zhao, Y., Seredych, M., Jagiello, J., Zhong, Q. & Bandosz, T. J. Insight into the mechanism of CO_2 adsorption on Cu–BTC and its composites with graphite oxide or aminated graphite oxide. *Chem. Eng. J.* **239**, 399–407 (2014).
99. Cao, Y., Zhao, Y., Lv, Z., Song, F. & Zhong, Q. Preparation and enhanced CO_2 adsorption capacity of UiO-66/graphene oxide composites. *J. Ind. Eng. Chem.* **27**, 102–107 (2015).
100. Qasem, N. A. & Ben-Mansour, R. Adsorption breakthrough and cycling stability of carbon dioxide separation from $CO_2/N_2/H_2O$ mixture under ambient conditions using 13X and Mg-MOF-74. *Appl. Energy* **230**, 1093–1107 (2018).
101. Broom, D. P. et al. Outlook and challenges for hydrogen storage in nanoporous materials. *Appl. Phys. A* **122**, 151 (2016).
102. Broom, D. P. et al. Concepts for improving hydrogen storage in nanoporous materials. *Int. J. Hydrog. Energy* **44**, 7768–7779 (2019).
103. Wang, T. C. et al. Ultrahigh surface area zirconium MOFs and Insights into the applicability of the BET theory. *J. Am. Chem. Soc.* **137**, 3585–3591 (2015).
104. Schoenecker, P. M., Carson, C. G., Jasuja, H., Flemming, C. J. J. & Walton, K. S. Effect of water adsorption on retention of structure and surface area of metal–organic frameworks. *Ind. Eng. Chem. Res.* **51**, 6513–6519 (2012).
105. Panella, B., Hirscher, M. & Roth, S. Hydrogen adsorption in different carbon nanostructures. *Carbon* **43**, 2209–2214 (2005).
106. Hirscher, M. Hydrogen storage by cryoadsorption in ultrahigh-porosity metal–organic frameworks. *Angew. Chem. Int. Ed.* **3**, 581–582 (2011).
107. Yang, Y., Chuah, C. Y. & Bae, T.-H. Polyamine-appended porous organic copolymers with controlled structural properties for enhanced CO2 capture. *ACS Sust. Chem. Eng.* **9**, 2017–2026 (2021).
108. Chuah, C. Y. & Bae, T.-H. Recent advances in mixed-matrix membranes for light hydrocarbon (C_1–C_3) separation. *Membranes* **12**, 201 (2022).
109. Chuah, C. Y., Goh, K. & Bae, T.-H. Enhanced performance of carbon molecular sieve membranes incorporating zeolite nanocrystals for air separation. *Membranes* **11**, 489 (2021).
110. Yang, Y., Chuah, C. Y. & Bae, T.-H. Highly efficient carbon dioxide capture in diethylenetriamine-appended porous organic polymers: investigation of structural variations of chloromethyl monomers. *J. Ind. Eng. Chem.* **88**, 207–214 (2020).
111. Bae, T.-H. et al. Evaluation of cation-exchanged zeolite adsorbents for post-combustion carbon dioxide capture. *Energy Environ. Sci.* **6**, 128–138 (2013).
112. Chuah, C. Y., Li, W., Yang, Y. & Bae, T.-H. Evaluation of porous adsorbents for CO_2 capture under humid conditions: The importance of recyclability. *Chem. Eng. J. Adv.* **3**, 100021 (2020).
113. Lee, J. et al. Separation of acetylene from carbon dioxide and ethylene by a water-stable microporous metal–organic framework with aligned imidazolium groups inside the channels. *Angew. Chem. Int. Ed.* **57**, 7869–7873 (2018).

ACKNOWLEDGEMENTS

This work is supported by the National Research Foundation of Korea (NRF) grant funded by the Korean government MSIT (Reference numbers: NRF-2021R1A2C3008570, NRF-2021M313A1084977, and NRF-2022R1A5A1033719). This work is also supported by the Murata Science Foundation (Cost Center 015ME0-297). The authors acknowledge the financial support by the Saudi Aramco-KAIST CO_2 Management Center.

AUTHOR CONTRIBUTIONS

The authors' contributions to this work are indicated as follows: Y.-J.P.: Conceptualization, Data Curation, Visualization, and Writing—Original Draft. H.L.: Conceptualization, Data Curation, Visualization and Writing—Original Draft. H.L.C.: Conceptualization, Data Curation, Visualization and Writing—Original Draft. M.C.T.: Writing—Review & Editing. C.Y.C: Conceptualization, Data Curation, Visualization, and Writing—Original Draft, Writing—Review & Editing. T.-H.B.: Writing —Review & Editing, Supervision, Funding acquisition. These authors contributed equally to this work: Yong-Ju Park, Hongju Lee & Hye Leen Choi. Corresponding authors are corresponded to Chong Yang Chuah or Tae-Hyun Bae.

COMPETING INTERESTS

The authors declare no competing interests.

ADDITIONAL INFORMATION

Supplementary information The online version contains supplementary material available at https://doi.org/10.1038/s41699-023-00425-w.

Correspondence and requests for materials should be addressed to Chong Yang Chuah or Tae-Hyun Bae.

Reprints and permission information is available at http://www.nature.com/reprints

Publisher's note Springer Nature remains neutral with regard to jurisdictional claims in published maps and institutional affiliations.